The Initial Conditions for Gravitational Collapse of a Core: An Extremely Young Low-Mass Class 0 Protostar GF 9-2

Ray S. FURUYA¹

Division of Physics, Mathematics, and Astronomy, California Institute of Technology

rsf@subaru.naoj.org

Yoshimi KITAMURA²

Institute of Space and Astronautical Science, Japan Aerospace Exploration Agency

kitamura@isas.jaxa.jp

and

Hiroko SHINNAGA³

Caltech Submillimeter Observatory, California Institute of Technology

shinnaga@submm.caltech.edu

ABSTRACT

We present a study of the natal core harboring the class 0 protostar GF 9-2 (bolometric luminosity $\simeq 0.3~L_{\odot}$, bolometric temperature $\lesssim 20~\mathrm{K}$; Wiesmeyer et al.) in the filamentary dark cloud GF 9 (distance = 200 pc) using the Nobeyama 45 m, CSO 10.4 m telescopes, and the OVRO mm-array. GF 9-2 stands unique in the sense that it shows H₂O maser emission (Furuya et al.), a clear signpost of

 $^{^1\}mathrm{Present}$ address: Subaru Telecope, National Astronomical Observatory of Japan, 650 North A'ohoku Place, Hilo, HI 96720

²3-1-1 Yoshinodai, Sagamihara, Kanagawa 229-8510, Japan

³111 Nowelo Street, Hilo, HI 96720

^{*}The preprint including figures with the original quality is available at http://subarutelescope.org/staff/rsf/publication.html

protostar formation, whereas it does not have a high-velocity large-scale molecular outflow evidenced by our deep search for ¹²CO wing emission. These facts indicate that GF 9-2 core is early enough after star formation so that it still retains some information of initial conditions for collapse. Our $350 \,\mu\mathrm{m}$ dust continuum emission image revealed the presence of a protostellar envelope with an extent of $\simeq 5400$ AU in the center of a molecular core $\simeq 0.08$ pc in size. The mass of the envelope is $\simeq 0.6~M_{\odot}$ from the 350 $\mu \mathrm{m}$ flux density, while LTE mass of the core is $\simeq 3~M_{\odot}$ from N₂H⁺, H¹³CO⁺, CCS, and NH₃ line observations. Combining visibility data from the OVRO mm-array and the 45 m telescope, we found that the core has a radial density profile of $\rho(r) \propto r^{-2}$ for $0.003 \lesssim r/\text{pc} \lesssim 0.08$ region. Molecular line data analysis revealed that the velocity width of the core gas increases inward, while the outermost region maintains a velocity dispersion of a few times of the ambient sound speed. The broadened velocity width can be interpreted as infall. Thus, the collapse in GF 9-2 is likely to be described by an extension of the Larson-Penston solution for the period after formation of a central star. We derived the current mass accretion rate of $\simeq 3 \times 10^{-5}~M_{\odot}$ year⁻¹ from infall velocity of $\simeq 0.3~{\rm km~s^{-1}}$ at $r \simeq 7000~{\rm AU}$. Furthermore, we found evidence that a protobinary is being formed at the core center. All results suggest that GF 9-2 core has been undergoing gravitational collapse for $\lesssim 5000$ years since the formation of central protostar(s), and that the unstable state initiated the collapse $\simeq 2\times 10^5$ years (the free-fall time) ago.

Subject headings: ISM: clouds — ISM: evolution — ISM: individual (GF 9–2, L 1082) — ISM: molecules — stars: formation — stars: pre-main sequence

1. Introduction

Stars form inside dense ($\simeq 10^5~{\rm cm}^{-3}$) and compact ($\simeq 0.1~{\rm pc}$) molecular cores (e.g., Myers & Benson 1983; Mizuno et al. 1994). One of the roles of such cores is to provide material for newly forming stars through dynamical accretion caused by gravitational collapse of the cores. For isolated low-mass star formation, two extreme paradigms for collapse of a core have been proposed. One is a slow, quasi-static model, while the other extreme is the dynamic, turbulent one. The former is represented by the Shu's similarity solution (Shu 1977), and the latter by the Larson-Penston's solution (Larson 1969; Penston 1969) which was extended for the period after a protostar formation by Hunter (1977) and Whitworth & Summers (1985). Hereafter, we refer to the latter extended solution as the Larson-Penston's solution. The two solutions are discriminated by radial density and velocity profiles of the

core at t=0. The Shu's solution (1977) sets the density profile of $\rho(r)=\frac{c_{\rm s}^2}{2\pi G}\,r^{-2}$ and is static (v(r)=0) at t=0 where $c_{\rm s}$ and G are the isothermal sound speed and the gravitational constant, respectively. At t=0, the collapse of the core begins at the center, which produces an expansion or rarefaction wave that propagates outward with the local sound speed. This model is referred to as the "inside-out" collapse (Shu 1977; Shu, Adams & Lizano 1987). On the other hand, the Larson-Penston's solution approaches the profile of $\rho(r) \simeq 4.4 \, \frac{c_{\rm s}^2}{2\pi G}\, r^{-2}$ and in infalling state $(v(r) \approx -3.28\,c_{\rm s})$ when a protostar is about to be born $(t\to -0)$, Hunter 1977; Shu 1977; Foster & Chevalier 1993). Thus the Larson-Penston solution, referred to as the "runaway" collapse, predicts a 48 times higher mass infall rate than the Shu's. At t>0, the both solutions have a free-fall region of $\rho(r) \propto r^{-3/2}$ which expands with sound speed for the Shu solution and with supersonic velocity for the Larson-Penston that accompanies no rarefaction wave.

Molecular line and dust continuum observations have identified a number of gravitationally bound starless cores (e.g., Mizuno et al. 1994), referred to as "preprotostellar" cores (Ward-Thompson et al. 1994). Thermal dust continuum emission imaging at mm and submm wavelengths revealed that radial density profiles of the preprotostellar cores have much flatter profiles than $\rho(r) \propto r^{-2}$ at radii smaller than a few thousand AU (e.g., Ward-Thompson et al. 1994; André et al. 1996). Molecular line studies measuring velocity field of the cores are also powerful tool to verify collapse models (e.g., Zhou 1992). For this purpose, it is the most important to search for a star-forming core which retains the initial conditions for the gravitational collapse, namely, a star-forming core at an extremely early evolutionary phase before dispersal by a large-scale molecular outflow. Furuya et al (1999, 2000) proposed that the intermediate-mass class 0 source S106 FIR is such an ideal core, because the source is characterized by (1) a cold SED (Richer et al. 1993), (2) H₂O maser emission, i.e., strong evidence for the presence of a protostar, and (3) absence of a large-scale high-velocity CO outflow.

We have successfully identified a low-mass counterpart, GF 9-2 by performing multiepoch H₂O maser survey (Furuya et al. 2001, 2003) and ¹²CO outflow mapping survey toward the selected low-mass protostars with the Nobeyama 45 m, SEST 15 m, and CSO 10.4 m telescopes (R. S. Furuya et al. in preparation). In our sample, GF 9-2 is the only protostar satisfying the above characteristics of (1)–(3). This protostar is located in the east-west filamentary dark cloud GF 9 where several YSOs are located every $\simeq 0.75$ pc in the plane of the sky (Schneider & Elmegreen 1979; Wiesemeyer 1997; the filament is crossidentified as Barnard 150 and Lynds 1082. The distance to GF 9-2 is estimated to be 200 pc by Wiesemeyer (1997). Wiesemeyer et al. (1997, 1999) identified GF 9-2 as class 0 and obtained bolometric temperature (T_{bol}) of ≤ 20 K and bolometric luminosity (L_{bol}) of $0.3L_{\odot}$. We believe that GF 9-2 offers unique opportunity to investigate the initial conditions for gravitational collapse of a star-forming core. This paper presents a detailed observational study of GF 9-2. In particular, we combined mm-interferometer and single-dish telescope visibility data to obtain high fidelity images of the core.

2. Observations

Toward GF 9-2, we observed dust continuum emission with the Caltech Submillimeter Observatory 1 (CSO) 10.4 m telescope (§2.1) and molecular line emission with the Nobeyama Radio Observatory (NRO) 45 m telescope (§2.2). We also carried out a deep search for molecular outflow using the 10.4 m and 45 m telescopes and used cm radio continuum data from the NRAO³ Very Large Array (VLA) archive data base to search for thermal radio jet (§2.4). The parameters for single-dish and interferometer observations are summarized in Tables 1 and 2, respectively.

2.1. Caltech Submillimeter Observatory 10.4 m Telescope

The 12 CO (3–2) line observations were done using the SIS receiver with position-switching mode in 2002 December. We used the 50 MHz bandwidth acousto-optical spectrometer (AOS). During the observations, the zenith opacities at 225 GHz ($\tau_{225~\rm GHz}$) ranged from 0.037 to 0.12. The telescope pointing was checked by observing the 12 CO (3–2) emission toward CRL 2688 every 1.5 hours, and the accuracy was better than 5". The observing grid was centered on the position of the 3 mm continuum source reported in Wiesemeyer et al. (1999) (R.A._{J2000} = $20^{\rm h}51^{\rm m}29$ ".5, Dec._{J2000} = $60^{\circ}18$ 38".0). In the data reduction, we removed spectra obtained with elevation angle of $\lesssim 30^{\circ}$ or with $T_{\rm sys} \geq 800$ K in single sideband (SSB).

¹The Caltech Submillimeter Observatory is operated by the California Institute of Technology under funding from the US National Science Foundation (AST 02-29008).

²Nobeyama Radio Observatory is a branch of the National Astronomical Observatory, operated by the Ministry of Education, Culture, Sports, Science and Technology, Japan.

³The National Radio Astronomy Observatory is a facility of the National Science Foundation operated under cooperative agreement by Associated Universities, Inc.

2.1.2. Imaging of 350 µm Continuum Emission with SHARCII

The SHARC II camera (Dowell et al. 2003) was used to obtain a 350 μ m continuum emission map in the box and Lissajous scan modes (Kovács 2006) in 2004 June. We used the Dish Surface Optimization System (DSOS) which actively corrects gravitational deformation of the main reflector of the telescope (Leong 2005). During our observations, $\tau_{225~\rm GHz}$ ranged from 0.045 to 0.08. The telescope focusing and pointing were checked every an hour by observing Neptune and Uranus. The measured beam size in HPBW was (8".9 \pm 0".2) \times (8".0 \pm 0".4) at P.A.= 93°. We estimated the positional accuracy of \lesssim 4" from maps of the pointing sources. For flux calibrations, we used the pointing data of Neptune that satisfied the condition of $\tau_{225\rm GHz}$ \times airmass \leq 0.1. We obtained a mean peak voltage ($V_{\rm peak}$) of 8.25 \pm 1.5 μ Volt toward Neptune over a pixel aperture ($A_{\rm pixel} = 4".9 \times 4".8$) of the detector. The measured voltage was converted into source intensity as $\frac{V_{\rm peak}}{A_{\rm pixel}} \propto \frac{S_{\nu}}{\Omega_{\rm b}}$ where S_{ν} denotes flux density per beam and $\Omega_{\rm b}$ beam solid angle. Since the brightness temperature of 63 K and the angular diameter of 2.6" for Neptune led to S_{ν} of 98.0 Jy at 350 μ m, we obtained a conversion factor of 3.2×10⁻⁶ Jy beam⁻¹ Volt⁻¹.

2.2. Nobeyama 45 m Telescope

2.2.1. Observations of ^{12}CO (1-0), $H^{13}CO^{+}$ and $HC^{18}O^{+}$ (1-0), and $C_{3}H_{2}$ $2_{12}-1_{01}$ Lines

We carried out simultaneous observations of ^{12}CO (1–0) and $\text{H}^{13}\text{CO}^{+}$ (1–0) lines using two SIS receivers (S100 and S80) with SSB filters in dual polarization mode in 2000 April. For the backend, we used the 8 arrays of AOS. All of the 45 m telescope observations were made in position switching mode, using an off-position of $(\Delta\alpha, \Delta\delta) = (-8.0, +10.0)$ to the 3 mm source. The pointing accuracy was better than 3". The daily variation of the receiver gains was estimated to be less than 10% in peak-to-peak, leading the corrected absolute flux uncertainty of 15%. In 2005 April, we made the simultaneous observations of the $\text{H}^{13}\text{CO}^{+}$ and $\text{HC}^{18}\text{O}^{+}$ (1–0) lines to measure optical depth of the $\text{H}^{13}\text{CO}^{+}$ line toward the 3 mm continuum source. At the same time, we also observed the ortho- C_3H_2 $2_{12}-1_{01}$ line.

2.2.2. Mapping Observations of ^{12}CO (1–0), $H^{13}CO^{+}$ (1–0) and SiO (2–1) Lines with BEARS

The mapping observations of the ^{12}CO (1–0), $H^{13}CO^{+}$ (1–0) and SiO (2–1) v=0 lines were carried out with the 25 BEam Array Receiver System (BEARS) in 2001 January

and April. For backend, we used digital spectrometers. We adopted correction factors provided by the observatory for relative gain differences among the 25 beams. The 12 CO and $\mathrm{H}^{13}\mathrm{CO}^{+}$ line data taken with the S100/S80 receivers with the SSB filters (§2.2.1) were used to determine the antenna temperature (T_{A}^{*}) scale for the BEARS which is not equipped with SSB filters. The telescope pointing accuracy was better than 3", and the uncertainty of temperature scale calibration was better than 20%.

2.2.3. Observations of
$$N_2H^+$$
 (1-0), CCS $4_3 - 3_2$ and CC⁸⁴S $4_3 - 3_2$ Lines

In 2003 December, we made the simultaneous N_2H^+ (1–0) and CCS 4_3-3_2 line observations with a grid spacing of 40", full-beam sampling for the CCS line. Subsequently, we carried out deeper integration of the N_2H^+ line with a spacing of 20", a full-beam sampling for the line. In addition, we observed CC³⁴S 4_3-3_2 line toward the 3 mm continuum source to estimate optical depth of the CCS line. The pointing accuracy and the uncertainty of flux calibration were the same as in §2.2.2.

2.2.4. Observations of NH₃ Inversion Lines at 23 GHz

We carried out mapping observations of the four inversion lines of NH₃ molecules at 23–24 GHz using the HEMT receiver (H20) with a dual circular polarization mode in 2001 April. We used the eight AOS arrays to receive both the polarizations of the 4 transitions and added the dual polarization data for each transition to improve S/N ratio. The telescope pointing accuracy was better than 5", and the uncertainty of temperature calibration was better than 20%.

2.3. Owens Valley Radio Observatory Millimeter Array

The aperture synthesis observations at 3 mm were carried out using the six-element OVRO mm array in the period from 2003 September to 2004 May with the 4 array configurations; 3 full-tracks at the C configuration, 5 at L, 2 at H, and 2 partial tracks at E (Table 2). The resultant projected baseline length ranged from 12.8 m to 224 m; our OVRO observations are insensitive to structures extended more than 54", corresponding to 0.052 pc at d = 200 pc. We used the 3 mm continuum source position reported in Wiesemeyer et al. (1999) as the phase tracking center. We observed the N_2H^+ (1–0) line in the upper sideband and the $H^{13}CO^+$ (1–0) line in the lower sideband. The velocity resolutions were 0.402 and

 0.108 km s^{-1} for the N_2H^+ and $H^{13}CO^+$ lines, respectively.

We used 3C 273, 3C 454.3 and 3C 84 as passband calibrators and J2038+513 as a phase and gain calibrator. The flux densities of J2038+513 were determined from observations of Uranus and Neptune. The measured flux densities were fairly stable in the range of 1.37 – 1.43 Jy at 86.7 GHz and of 1.26 – 1.38 Jy at 93.2 GHz. The uncertainty in our flux calibration was estimated to be 10%. To minimize atmospheric phase fluctuation errors, we removed all the GF 9-2 data taken in the switching cycles when the coherency of the calibrator was less than 70%. The data were calibrated and edited using the MMA and MIRIAD packages. For the continuum data, we merged the visibilities in both the sidebands to construct an image; the final center frequency is 89.964 GHz. Images of both the line and continuum were constructed using the AIPS package.

Since an interferometer does not have sensitivity to structures extended more than the largest fringe-spacing given by the shortest projected baseline length, we used the 45 m telescope maps to recover filtered-out emission in our OVRO mm-array observations (Table 3; Appendix A). After combining interferometer and single-dish visibilities, we CLEANed maps using the task IMAGR in the AIPS package. The parameters of the final maps are given in Table 3.

2.4. Very Large Array

We used the 8435 MHz continuum emission image of GF 9-2 from the VLA archive database. The data were originally taken by Wiesemeyer et al. in 1997 July with the Carray configuration (Table 2). The flux densities of calibrators of J2022+616 and J2055+613 were determined from observations of the standard calibration sources of 3 C286 and 3 C48, and the uncertainty in the final flux calibration was better than 20%.

3. Results

3.1. Continuum Emission

3.1.1. Non-Detection of Free-Free Emission at 8.4 GHz

No radio continuum emission from ionized gas is detected toward GF 9-2 through our VLA C-configuration search at 8.4 GHz ($\lambda = 3.6$ cm). The attained 3σ sensitivity is 0.11 mJy beam⁻¹, leading to the upper limit of the 3.6 cm continuum luminosity of 0.005 mJy

kpc² within the beam. This upper limit is lower than the luminosity of the least luminous thermal cm continuum emission (see Figure 3 of Cabrit & Bertout 1992; Furuya et al. 2003). Since cm continuum emission toward protostars is usually attributed to free-free emission from ionized gas produced by strong shocks of protostellar jets, the lack of the cm emission in GF 9-2 suggests that a jet, if exists, is not so powerful to ionize ambient gas.

3.1.2. Thermal Dust Emission at 3 mm and $350 \mu m$

In Figure 1, we present a comparison between the continuum emission maps at $350\,\mu\mathrm{m}$ taken with the SHARC II camera and at 3 mm with the OVRO mm-array. The maps show that a 3 mm point source is embedded in the extended $350\,\mu\mathrm{m}$ emission. The peak position of the 3 mm emission is R.A.= $20^{\rm h}51^{\rm m}29.^{\rm s}827$, Decl.= 60° 18′ 38″.06 in J2000. The $350\,\mu\mathrm{m}$ emission has a size of $33''.0 \times 22''.5$, corresponding to 6600×4500 AU which is comparable to the typical size of a protostellar envelope (≤ 6000 AU; Mundy, Looney & Welch 2000). It is most likely that the $350\,\mu\mathrm{m}$ emission traces a protostellar envelope, whereas the 3 mm emission is more compact, perhaps a protoplanetary disk. We assume that a protostar is located at the peak of the 3 mm emission. By integrating the emission inside the 3σ contours, we obtain the total flux densities S_{ν} (Table 4). Here we consider that the 3 mm emission has negligible contribution from optically thin free-fee emission because our non-detection of the 8.4 GHz continuum emission gives a 3σ upper limit of 0.090 mJy at 3 mm for the free-free emission by extrapolating with $I_{\nu} \propto \nu^{-0.1}$.

Assuming that the dust continuum emission is optically thin, we estimate the envelope mass $(M_{\rm env})$ from the 350 μ m total flux density. We used an equation of $M_{\rm env} = \frac{S_{\nu}d^2}{\kappa_{\nu}B_{\nu}(T_{\rm d})}$ where κ_{ν} is the dust mass opacity coefficient, $T_{\rm d}$ the dust temperature, and $B_{\nu}(T_{\rm d})$ the Planck function. Assuming that dust and gas are well coupled, we adopt $T_{\rm d}$ of 9.5 K, a mean excitation temperature $(T_{\rm ex})$ obtained from the N₂H⁺ (1–0) data (described in §4.1.1). The value of κ_{ν} at 350 μ m is estimated by the usual form of $\kappa_{\nu} = \kappa_{\nu 0} (\nu/\nu_0)^{\beta}$. Here we used two sets of the representative κ_0 and β values reported in preprotostellar cores (case I) and in envelopes around class 0/I protostars (case II), because κ_0 is known to change with evolutionary class. Recall that the source is very likely to be in an evolutionary phase between a preprotostellar core and a class 0 protostar. Given κ_0 of 0.005 cm² g⁻¹ at ν_0 = 231 GHz (Preibish et al. 1993, André, Ward-Thompson, & Motte 1996) and β of 2.0 (Beckwith, Henning & Nakagawa 2000, and references therein) for case I, we have κ of 0.069 cm² g⁻¹ at 850 GHz. On the other hand, given κ_0 of 0.01 cm² g⁻¹ at 231 GHz (Ossenkopf & Henning 1994) and β of 1.0 (Beckwith et al. 2000) for case II, we have κ of 0.037 cm² g⁻¹ at 850 GHz. Finally, we obtain the total masses of 0.4 M_{\odot} for case I and 0.8 M_{\odot} for case II. The inferred

mass range is comparable to the least massive envelope masses in class 0 sources known to date, i.e., $M_{\rm env} \simeq 0.5~M_{\odot}$ for HH25 MMS-MM and L1157 MM (André, Ward-Thompson & Barsony 1993, hereafter AWB93). Using the source size ($\Omega_{\rm s}$) of 957 arcsec² inside the 3σ level contour, and $M_{\rm env}$, a mean column density of H₂ molecules, $N({\rm H_2})_{8''}$, is estimated to be 4.2×10^{22} and 7.8×10^{22} cm⁻² for cases I and II, respectively. These are converted into a mean optical depth of $\simeq 7 \times 10^{-3}$ for both the cases, justifying our assumption of optically thin emission.

3.2. Molecular Line Emission

3.2.1. Spectral Profile of the Molecular Line Emission toward the Center

In Figure 2, we present the spectra of ^{12}CO (1-0), (3-2), N_2H^+ (1-0) $F_1,F=0,1-1,2$, ${\rm H^{13}CO^{+},\ HC^{18}O^{+}\ (1-0),\ C_{3}H_{2}\ 2_{12}-1_{01},\ CCS,\ CC^{34}S\ 4_{3}-3_{2},\ and\ SiO\ (2-1)\ \it{v}\,=\,0\ lines}$ toward the 3 mm continuum source. Figure 3 represents the N₂H⁺ (1–0) spectrum to show all the hyperfine components. We summarize the parameters of these spectra in Table 5. Intrinsic velocity width $(\Delta v_{\rm int})$ in the table indicates the velocity width corrected for line broadening (where appropriate) due to instrumental velocity resolution and optical depth of the line (Phillips et al. 1979). The ¹²CO (1–0) spectrum shows a broad line width of $\simeq 2 \text{ km s}^{-1}$ in full-width at half maximum (FWHM). The 12 CO (3–2) spectrum displays a blueshifted wing emission up to $V_{\rm LSR} \simeq -6~{\rm km~s^{-1}}$ and a less prominent red wing up to \simeq $+0.5 \text{ km s}^{-1}$. The spectrum has a central dip at $V_{LSR} = -2.8 \text{ km s}^{-1}$, while the high density gas tracers of N₂H⁺, H¹³CO⁺, C₃H₂, and CCS show their peaks around the dip of the ¹²CO (3–2) spectrum. Such a coincidence indicates that the two peaks in the ¹²CO (3–2) spectrum arise from self-absorption, and not from two velocity components along the line-of-sight. At ¹²CO (1–0), the self-absorption is broad; the peak in the redshifted side is almost missing, and only the blueshifted peak is seen. Here, we define systemic velocity (V_{sys}) of the cloud core as $-2.5 \ \mathrm{km \ s^{-1}}$, the peak velocity of the CCS $4_3 - 3_2$ line, because the line has a single sharp peak and is optically thin (described in $\S4.1.4$). In addition, the $H^{13}CO^{+}$ and $N_{2}H^{+}$ lines show similar line profiles in the sense that they have stronger blue peaks, a typical signature of infall (e.g., Walker et al. 1986). The C₃H₂ spectrum shows a flat-top shape. Lastly, we point out that no molecular line emission is seen around $V_{\rm LSR} = 5.7~{\rm km~s^{-1}}$ where we detected the weak H₂O masers (Furuya et al. 2003). This may suggest that the masers are excited in shocked region impacted by a possible protostellar jet because such jet-origin water masers in low-mass YSOs usually do not appear around their cloud velocities (Terebey, Vogel & Myers 1992; Chernin 1995; Claussen et al. 1998; Moscadelli et al. 2006).

3.2.2. Single-Dish Maps of High Density Gas

Figure 4 illustrates total integrated intensity maps of the high density gas tracers of $\mathrm{H^{13}CO^{+}}$ (1–0), CCS 4_3 – 3_2 , $\mathrm{N_2H^{+}}$ (1–0), and $\mathrm{NH_3}$ lines taken with the 45 m telescope. We integrated all of the hyperfine components for the nitrogen-bearing molecules having hyperfine structures. The four lines show similar overall structures. It is very likely that all of the molecular lines trace a natal cloud core of GF 9-2. The highest contour of the $\mathrm{H^{13}CO^{+}}$ and $\mathrm{N_2H^{+}}$ emission show east-west (EW) elongation. In addition, the $\mathrm{N_2H^{+}}$ map shows a higher degree of central concentration than the $\mathrm{H^{13}CO^{+}}$ and CCS maps with comparable beam sizes. The 3 mm dust continuum emission is located at the densest innermost region of the core, although its position is slightly displaced to the east of the $\mathrm{H^{13}CO^{+}}$ and $\mathrm{N_2H^{+}}$ peaks.

Figure 5 shows velocity channel maps of the $\mathrm{H^{13}CO^{+}}$ (1–0) and $\mathrm{N_{2}H^{+}}$ (1–0) $\mathrm{F_{1},F=0,1-1,2}$ lines observed with the 45 m telescope; the latter transition is not blended with the other 6 hyperfine components. The $\mathrm{H^{13}CO^{+}}$ channel maps exhibit a velocity gradient along the major axis of the core; the redshifted gas dominantly lies to the NE of the 3 mm source, whereas the blueshifted one to the SW.

3.2.3. Combined OVRO mm array and Nobeyama 45 m Telescope Data

Figure 6 shows the combined N_2H^+ and $H^{13}CO^+$ images together with the original 45 m and OVRO maps, and Figure 7 shows channel maps of the combined data. We note that the OVRO and combined images are insensitive to the emission outside the fields of view of the OVRO array due to primary beam attenuation of the element antennas, and that the combined $H^{13}CO^+$ and N_2H^+ images are $\simeq 4$ and 15 times less sensitive compared to the 45 m maps, respectively. The OVRO images in Figure 6 trace the innermost region of the core and clearly show that both the N_2H^+ and $H^{13}CO^+$ peaks are shifted to the west of the 3 mm source. The combined images in Figure 6 show that there is a centrally peaked feature which is elongated along EW in the smaller scale and that intensity of the two lines decreases with increasing the radial distance from the center. However, contrary to Figure 5, one cannot see a well-defined velocity gradient in the combined channel maps of the $H^{13}CO^+$ emission (Figure 7).

3.3. Search for Molecular Outflows and Jets

3.3.1. Search for CO Outflow

Figure 8 compares the blue- and redshifted ¹²CO (1–0) and (3–2) emission integrated over the velocity ranges shown in Figure 2. In the figure, no highly-collimated high-velocity "jet-like" outflow typically seen in class 0 sources (Bachiller 1996, and references therein) is identified toward the 3 mm source, although formation of protostar in GF 9-2 core is strongly suggested by the H₂O masers. This is because the terminal velocity of the blueand redshifted emission, shifted by only $\simeq 3 \text{ km s}^{-1}$ to V_{sys} (Figure 2), is too small to be interpreted as the line-of-sight components of CO outflow velocity $(V_{\rm flow})$ in class 0 sources (e.g., $V_{\rm flow} \simeq 50~{\rm km~s^{-1}}$ for VLA 1623; André et al. 1990). Instead, a condensation of the low-velocity redshifted gas lies to the south of the 3 mm source in the (3–2) map. A similar condensation is marginally seen in the redshifted (1–0) map, but seems to be a part of the large-scale natal filament. These red condensations might represent a compact low-velocity outflow which has just launched from a protostar. On the other hand, a patchy distribution of the blueshifted (3–2) gas is observed, partly because of the quality of spectral baselines. The blueshifted (1–0) map shows a ridge to the NE of the 3 mm source, and is connected to the EW natal filament, whereas the blueshifted (3–2) emission seems to be resolved into two peaks in the core center.

First, we estimate an upper limit to the mass of the high-velocity outflow gas. Since the CO emission is very likely to be optically thick, we consider that the peak brightness temperature gives a good estimate of $T_{\rm ex}$, assuming that the emission fills the beam. We derive $T_{\rm ex}$ of 5.9 K from the (1–0) and 6.9 K from (3–2) transitions, considering the cosmic background temperature ($T_{\rm bg}=2.7$ K). We attained 3σ upper limits of 12 and 79 mK for the (1–0) and (3–2) transitions, respectively, with a velocity width of 50 km s⁻¹ which is a typical velocity of high-velocity jet-like outflows associated with class 0 sources (e.g., Bachiller 1996), although Figure 2 shows terminal velocity is $\simeq 3$ km s⁻¹. Given the mean value of $T_{\rm ex}=6.4$ K and [CO]/[H₂] $\simeq 10^4$ (Dickman 1978), we convert these upper limits into mass per lobe ($M_{\rm lobe}$) of $6.7 \times 10^{-5} M_{\odot}$ for (1–0) and $1.7 \times 10^{-3} M_{\odot}$ for (3–2). Clearly, these 3σ detection limits in mass are sufficient to identify any of the CO outflows associated with class 0 sources known to date (e.g., Richer et al. 2000).

Next, we estimate mass of the possible low-velocity ($\simeq 3 \text{ km s}^{-1}$) outflow suggested by the weak wing emission in Figure 2 and by the redshifted condensation in Figure 8. The extents of the lobes are approximately 0.053 and 0.032 pc for the blue- and red ones from the 3 mm source, respectively. Given $T_{\rm ex} = 6.4 \text{ K}$, we obtain $M_{\rm lobe}$ of $1.6 \times 10^{-4} M_{\odot}$ for the blue and $2.6 \times 10^{-4} M_{\odot}$ for the red. These lobe masses are considerably smaller than those

in class 0 sources.

3.3.2. Non-Detection of Shock Excited SiO Emission

Thermal SiO emission is believed to be one of the most reliable shock tracers associated with molecular outflow (e.g., Codella, Bachiller & Reipurth 1999) because the destruction of dust grains releases silicon into the gas-phase and silicon is rapidly oxydized to produce SiO (e.g., Schilke et al. 1997). No evidence of outflow shocked regions is found in the SiO emission over a 0.22 pc \times 0.14 pc region centered on the 3 mm continuum source. The searched area is sufficiently large to detect such SiO emission enhanced at leading edge of the possible outflow lobe younger than dynamical age of \lesssim 0.053 pc/3 km s⁻¹ \simeq 1.7 \times 10⁴ years. This result suggests that the compact low-velocity outflow (§3.3.1) is not powerful enough to excite thermal SiO emission.

4. Analysis

4.1. Column Density of the Core

4.1.1.
$$N_2H^+$$
 (1-0)

To estimate the column density of N_2H^+ ($N_{N_2H^+}$), we analyze the hyperfine structure (HFS) due to the electric quadrupole moment of the N nucleus. We performed least-squares fitting to each spectrum by applying a model spectrum having seven Gaussian components assumed to have the intrinsic intensity ratios in local thermodynamic equilibrium (LTE) at the limit of $\tau=0$ (Cazzoli et al. 1985). The details of the HFS analysis and the column density calculations are described in Appendix B.1. The free parameters are $T_{\rm ex}$, velocity width ($\Delta v_{\rm FWHM}$), LSR velocity of the brightest hyperfine (HF) component (J=1-0 F₁,F = 2,3-1,2 transition at 93173.809 MHz), and the sum of the optical depths of the components ($\tau_{\rm tot}$). We have presented an example N_2H^+ spectrum toward the 3 mm peak position in Figure 3. We used only the single dish data because the velocity resolution is 3.4 times higher than that of the combined data. The parameters of the best-fit model profiles for the HF spectrum, shown by the green histogram, are summarized in Table 5.

To perform HFS analysis on the combined data, we create a spectrum at each map pixel from the 3D cube data. The pixel size is set to be 0.9, the maximum size to avoid aliasing in the Fast Fourier Transformation (FFT) of the combined visibilities, whereas that for the 45 m data is set to be 5. We obtained reasonable fitting results from 262 and 1776 spectra

for the 45 m and combined data, respectively. For the remaining spectra, we failed to achieve a fit because the weakest HF component of $F_1,F=0,1-1,2$ whose intrinsic intensity is 0.111 times of that of the brightest $F_1,F=2,3-1,2$ did not have S/N-ratio higher than 5.

Figure 9 shows total column density maps of N_2H^+ calculated from the 45 m and combined data. To produce Figure 9, we calculated $N_{N_2H^+}$ at each pixel using Eq.(B7) where we used $T_{\rm ex}$, $\tau_{\rm tot}$, and intrinsic velocity width, $\Delta v_{\rm int}$, derived from the HFS analysis of the N_2H^+ spectrum at a pixel. The 45 m $N_{N_2H^+}$ map shows that the core has the densest region at the center, and that the column density decreases outward. The combined N_2H^+ map shows that the extent of the densest central region is smaller than the 45 m beam size. The region has an approximate extent of 10" (corresponding to 0.01 pc) and $N_{N_2H^+}$ of $\gtrsim 10^{14}$ cm⁻². Notice that the 3 mm source is shifted by 6" to the east of the $N_{N_2H^+}$ peak.

To obtain fractional abundances of the probe molecules in §4.2, we recalculate $N_{\rm N_2H^+}$ with various beam sizes. We smoothed the 45 m data by 40" and 80" beams for $r \leq 20$ " and 40" regions centered on the 3 mm source. Table 6 summarizes the calculated $N_{\rm N_2H^+}$ and compares CCS and NH₃ column densities. We also reconstructed N₂H⁺ images from the combined visibilities by giving the SHARC II beam as a synthesized beam size and calculated $N_{\rm N_2H^+}$ inside the 3 σ level contour of the 350 μ m emission.

In addition, we analyzed the N_2H^+ line data with the 45 m telescope to use the line as a temperature probe for the other molecules because the N_2H^+ HFS analysis gives rather accurate estimates of $T_{\rm ex}$ and the spatial resolution for N_2H^+ is the highest among our data. We analyzed N_2H^+ spectra inside the region enclosed by the half maximum, i.e., 50% level contour to the peak intensity and obtained mean $T_{\rm ex}$ of 9.5 ± 1.9 K (Table 5). We assume that the core has a temperature of 9.5 K and use the temperature to calculate the column density of the other molecules. Note that the adopted temperature is higher than the range of 5 to 7 K for the ambient gas inferred from the 12 CO (3–2) and (1–0) emission (§3.3.1).

4.1.2.
$$H^{13}CO^{+}$$
 (1-0)

To estimate the column density of $\mathrm{H^{13}CO^{+}}$ ($N_{\mathrm{H^{13}CO^{+}}}$), we analyzed both the 45 m telescope and combined data. We firstly estimate optical depth ($\tau_{\mathrm{H^{13}CO^{+}}}$) of the $\mathrm{H^{13}CO^{+}}$ (1–0) line toward the core center from an antenna temperature ratio of $T_{\mathrm{A}}^{*}(\mathrm{H^{13}CO^{+}})/T_{\mathrm{A}}^{*}(\mathrm{HC^{18}O^{+}})$. Here, we assume that the beam filling factors, T_{ex} , and the telescope beam efficiencies are the same for the two isotope lines. In addition, we assume that the solar abundance ratio $\frac{[^{13}\mathrm{Cl}]}{[^{16}\mathrm{Ol}]}$ of 5.5 is applied to the $[\mathrm{H^{13}CO^{+}}]/[\mathrm{HC^{18}O^{+}}]$ ratio. Using the peak T_{A}^{*} of 440 mK for the $\mathrm{H^{13}CO^{+}}$ line in Table 5 (T_{mb} is converted into T_{A}^{*} by multiplying η_{mb} shown in Table

1) and the 1.5σ upper limit of 39 mK in $T_{\rm A}^*$ for the HC¹⁸O⁺ line (Table 1), we found that the H¹³CO⁺ line is optically thin (< 0.1; Table 5). Given $\tau_{\rm H^{13}CO^+}$ of < 0.1 and $T_{\rm ex}$ of 9.5 K (§4.1.1), we obtained $N_{\rm H^{13}CO^+}$ from the 45 m and combined data (Table 6) by using Eqs.(B9) and (B10) (see Appendix B.2), where the SHARC II beam was used as a synthesized beam to calculate $N_{\rm H^{13}CO^+}$ inside the 3σ contour of the 350 μ m emission.

4.1.3.
$$C_3H_2$$
 $2_{12} - 1_{01}$

For calculating C_3H_2 column density $(N_{C_3H_2})$ traced by the $2_{12}-1_{01}$ transition, we followed the calculations by Benson, Caselli & Myers (1998) (see their Appendix A2). We observed C_3H_2 only toward the core center. We estimated the optical depth using Eq.(17) by Benson et al. (1998) of $\tau_{C_3H_2} = \ln\left(\frac{T_{\rm ex}-T_{\rm mb}}{T_{\rm ex}-T_{\rm mb}-T_{\rm bg}}\right)$; $\tau_{C_3H_2} = 0.34$ for $T_{\rm mb}$ of 1.1 K, assuming $T_{\rm ex} = 9.5$ K (§4.1.1). We derived $\Delta v_{\rm int}$ (Table 5) from the second order moment of the spectrum because the line profile is not a single Gaussian (see Figure 2). Finally, a mean C_3H_2 column density is estimated to be $(2.4 \pm 0.3) \times 10^{13}$ cm⁻² (Table 6).

4.1.4.
$$CCS 4_3 - 3_2$$

In the similar manner as the H¹³CO⁺ analysis, we estimated the CCS column density $(N_{\rm CCS})$ using Eq.(B11). We obtain $\tau_{\rm CCS}$ of 0.94 (Table 5) from a ratio of $T_{\rm A}^*({\rm CCS})/T_{\rm A}^*({\rm CC}^{34}{\rm S})$ = 15.2 which is derived from the peak $T_{\rm A}^*$ of 560 mK for CCS (Table 5) and a 1.5 σ upper limit of 37.5 mK for CC³⁴S (Table 1). Here we adopt the solar abundance ratio [³²S]/[³⁴S] of 23. Given $\tau_{\rm CCS}$ of 0.94 and $T_{\rm ex}$ of 9.5 K, we obtain $N_{\rm CCS}$ of $(1.5 \pm 0.2) \times 10^{13}$ cm⁻² toward the core center with a 40" beam (Table 6).

$$4.1.5.$$
 NH_3 $(1,1)$

We present spectral line profiles of the NH₃ (J, K) = (1, 1) and (2, 2) lines in Figure 10. The (1, 1) spectrum consists of five groups of the lines. The most intense emission in the (1, 1) transition, the central group which contains eight of HF lines, has a peak $T_{\rm mb}$ of 640 mK, whereas no (2, 2) emission is seen above our 3σ level detection threshold $(T_{\rm mb} = 210$ mK). Neither the (3, 3) nor (4, 4) emission was detected.

To estimate NH₃ column density (N_{NH_3}) , we followed the previous works, e.g., Winnewisser, Churchwell & Walmsley (1979), Ungerechts, Walmsley & Winnewisser (1980),

Stutzki, Ungerechts & Winnewisser (1982), and Ho & Townes (1983). We analyzed the spectra taken inside the 50% level contour of the total intensity map (Figure 4d). In the similar manner as the N_2H^+ HFS analysis, our ammonia HFS analysis gives τ_{tot} and Δv_{FWHM} , and the LSR-velocity of the strongest HF component. The brightest HF emission has optical depth of $\simeq 1.6$ toward the core center (Table 5). Here we assume that the beam filling factor is unity. It is known that rotational temperature ($T_{r,21}$) between the (1,1) and (2,2) transitions and the kinetic temperature (T_k) agree well with each other for high density ($\gtrsim 10^6$ cm⁻³) and cold ($\lesssim 10$ K) gas (Tafalla et al. 2004). We therefore assume $T_{r,21} = T_k$, and that T_k is equal to $T_{ex}(N_2H^+)$ of 9.5 K (§4.1.1). Now we calculate a mean column density of $(1.6 \pm 0.6) \times 10^{14}$ cm⁻² for the NH₃ molecule in the (1,1) state inside the 50% level contour of the total integrated intensity map by inverting Eq.(2) of Ungerechts et al. (1980) We consequently obtained total NH₃ column density from the (1,1) column density by Eq.(2) of Winnewisser et al. (1979) (Table 6).

4.2. Fractional Abundances of the Molecules in the Core

To calculate mass (M_{LTE}) of the core from the column densities (§4.1), we need to find the fractional abundances (X_m) of the probe molecules to H₂ molecules. Such an abundance is known to vary under different physical and chemical conditions. Bergin & Langer (1997) theoretically predicted that all molecules are depleted in some degree from gas phase for high densities of $n(H_2) \gtrsim 10^6$ cm⁻³, regardless of dynamical evolutionary phases. The depletion of sulfur-bearing molecules such as CS, SO, and CCS is particularly sensitive to the density increase because they tend to stick to both H₂O and CO ice covered grains. In contrast, nitrogen-bearing molecules of NH₃ and N₂H⁺ do not seem to be susceptible to freezing out on the grain surface (Bergin & Langer 1997). This prediction is confirmed by the recent observations toward starless cores, e.g., Tafalla et al. (2002) who showed that N₂H⁺ and NH₃ column densities correlate better with the dust column density than molecules such as CO and CS. This characteristic, coupled with high angular resolution, makes N₂H⁺ ideal as a reference molecule. In addition, we believe that the possible low-velocity compact outflow does not affect our discussion about molecular abundances, considering our findings from radial density profile, position-velocity diagrams and velocity width maps of the core (described in $\S4.4$ and $\S4.5$).

4.2.1. N_2H^+ and $H^{13}CO^+$

The abundances of N_2H^+ and $H^{13}CO^+$ are estimated through comparison to the mean H_2 column density, $N(H_2)_{8''}$, derived from the 350 μ m continuum flux with the SHARC II beam (§3.1.2). Because the extent of the 350 μ m emission is approximately 4 times smaller than those of the N_2H^+ and $H^{13}CO^+$ emitting regions, such a comparison is possible only in the common innermost region of the core. Comparing the $N(H_2)_{8''}$ with the N_2H^+ and $H^{13}CO^+$ column densities with the SHARC II beam size (Table 6), we obtained $X(N_2H^+)_{8''} = (9.5 \pm 5.0) \times 10^{-10}$ and $X(H^{13}CO^+)_{8''} = (8.5 \pm 4.7) \times 10^{-12}$ (Table 7). Note that the errors in X_m are mostly due to the uncertainties in κ_{ν} (§3.1.2).

We argue that N_2H^+ in GF 9-2 is not depleted, whereas $H^{13}CO^+$ is depleted. Our estimate of $X(N_2H^+)_{8''}$ is comparable to those in the following studies. Womack et al. (1992) obtained a typical value of $X(N_2H^+)=7\times10^{-10}$ in the dark cloud cores TMC-1 and L134 N ($\theta_{HPBW}=70''$). Benson et al. (1998) derived (7 ± 4) \times 10^{-10} from a Haystack 37 m (22") survey towards 60 low-mass cores. Caselli et al. (2002) reported (3 ± 2) \times 10^{-10} from a FCRAO 13.6 m (54") mapping survey towards 34 dense cores. Tafalla et al. (2002) reported the range of (0.75-2.4) \times 10^{-10} toward 5 starless cores using the FCRAO. The consistency between our measurements with 8" beam and those with 22", 54", and 70" beams suggest that N_2H^+ in GF 9-2 is not depleted at the core center. On the other hand, $X(H^{13}CO^+)_{8''}$ in GF 9-2 is by a factor of almost 6 smaller than the lowest abundances in other similar cores measured with 67" beam (Table 9 by Butner et al. 1995), e.g., 5.6×10^{-11} for B 335 (class 0) and 5.4×10^{-11} for L 1495 (class I). This fact suggests that $H^{13}CO^+$ in GF 9-2 is very likely to be depleted at the center, although we need to verify the radial variation of $X(H^{13}CO^+)$.

4.2.2. C_3H_2 , CCS and NH_3

Using the $X(N_2H^+)_{8''}$ as a reference value, we estimated the abundances of C_3H_2 , CCS and NH₃. For this purpose, we assumed that N_2H^+ in GF 9-2 does not have radial abundance variation. Recall that Tafalla et al. (2002) reported that N_2H^+ abundances are spatially constant in the 5 starless cores they surveyed. Given the $X(N_2H^+)_{8''}$ and a column density ratio of $N(C_3H_2)/N(N_2H^+)$ with 20" beam (Table 6), we obtained $X(C_3H_2)_{20''}$ of $(2\pm 1)\times 10^{-10}$ (Table 7). Similarly we obtained $X(CCS)_{40''}$ of $(5\pm 3)\times 10^{-10}$ from an $N(CCS)/N(N_2H^+)$ ratio for $r \leq 20''$, and $X(NH_3)_{80''}$ of $(2\pm 1)\times 10^{-8}$ from an $N(NH_3)/N(N_2H^+)$ ratio for $r \leq 40''$.

The $X(C_3H_2)_{20''}$ value in GF 9-2 would fall at the lower end of the $X(C_3H_2)$ range, $(3.2-40)\times 10^{-10}$, obtained from the survey toward dense dark clouds with 54" beam (Cox,

Walmsley & Güsten 1989), although the beam sizes differ by a factor of ~ 2.5 . The estimated $X(CCS)_{40''} = (5 \pm 3) \times 10^{-10}$ is consistent with those of the starless cores measured with comparable beam sizes, i.e., 5.8×10^{-10} in TMC-1D and 4.9×10^{-10} in L 1498 with 45'' - 53'' beams (Wolkovitch et al. 1997), although smaller than $(8 \pm 3) \times 10^{-9}$ with $\sim 52''$ beam in L 1521 F (Shinnaga et al. 2004). On the other hand, the $X(CCS)_{40''}$ in GF 9-2 is found to be larger than those in the representative class 0 sources B 1 and B 335 ($\simeq 9 \times 10^{-11}$ and $\simeq 1.6 \times 10^{-10}$, respectively) reported in Lai & Crutcher (2000) with $\simeq 30''$ BIMA beam. Lastly, the $X(NH_3)_{80''} = (2 \pm 1) \times 10^{-8}$ in GF 9-2 is somewhat smaller than the mean value derived from the large compilation of literature toward the cores in the Taurus and Ophiucus regions $((4.0^{+2.3}_{-0.8}) \times 10^{-8}$; Table B10 of Jijina et al. 1999), but is comparable to the range of $(0.4 - 2.3) \times 10^{-8}$ for the 5 starless cores surveyed by Tafalla et al. (2002).

Here we wish to discuss age of the GF 9-2 core in terms of chemical evolution. Suzuki et al. (1992) analyzed their 45 m telescope CCS survey data by developing a chemical evolutionary model, and concluded that CCS is the most abundant in the early evolutionary stage for a quiescent dark cloud core, whereas NH₃ is less abundant and becomes abundant in the later evolutionary stage. Aikawa et al. (2001) advanced such a model for a dynamically collapsing core and pointed out that N_2H^+ shows similar chemical evolution as NH₃. Comparing the $X(NH_3)_{80''}$ and $X(CCS)_{40''}$ with Figure 16 in Suzuki et al. (1992) in conjunction with Figure 5 of Aikawa et al. (2001), we argue that GF 9-2 core has experienced $10^5 - 10^6$ years since the diffuse stage. Because of the large uncertainty in our abundance estimate, we have limited our discussion to the 3 molecules whose abundance variation with time are large enough to compare with our results.

4.3. LTE Mass of the Core

Using the column densities of the N₂H⁺, H¹³CO⁺, CCS, and NH₃ lines (§4.1) and their fractional abundances (§4.2), we now calculate the LTE mass ($M_{\rm LTE}$) of the gas in the area (\mathcal{A}) enclosed by the 50% level contour of each total integrated intensity map of Figure 4 (see Table 8). The mass is given by $M_{\rm LTE} = \mu m_{\rm H} \cdot \frac{N_{\rm m}}{X_{\rm m}} \cdot \mathcal{A}$ where μ is the mean molecular weight (2.33 for [He]= 0.1[H]) and $m_{\rm H}$ is the atomic mass of hydrogen. The obtained LTE masses range from 1.2 to 4.5 M_{\odot} .

4.4. Radial Column Density Profile of the Core

We derive radial column density profile of GF 9-2 core using the N₂H⁺ column density maps. Recall that the N₂H⁺ in GF 9-2 is unlikely to be depleted over the full extent of the core, whereas the H¹³CO⁺ may be depleted (§4.2.1). We assume that the core is spherical. To azimuthally average the column density maps, we take the N₂H⁺ emission peak as the center. Figure 11 represents the resultant column density profiles. The profiles can be well fitted by a power-law function of $N(r) = N_0(\frac{r}{r_0})^{-p}$ where p is the power-law index, and N_0 is the column density at $r = r_0 = 1''$. By minimizing the χ^2 values, we obtained the best-fit parameters of $p = 1.0 \pm 0.1$ and $N_0 = (7.3 \pm 1.1) \times 10^{14}$ cm⁻² for the combined data, and $p = 1.1 \pm 0.2$ and $N_0 = (8.5 \pm 2.5) \times 10^{14}$ cm⁻² for the 45 m telescope data. The two fitting results show good consistency within uncertainties, indicating that a negligible amount of the dense gas has been evacuated by the possible compact outflow in the innermost region of $r \lesssim 3''$.

4.5. Velocity Structure of the Core

4.5.1. Overall Velocity Structure

To examine the velocity structure of GF 9-2 core, we made position-velocity (PV) diagrams using the 45 m N₂H⁺ (1–0) F₁,F=0,1–1,2 and H¹³CO⁺ (1–0) line data (Figure 12). We also overlaid PV diagrams made from the combined H¹³CO⁺ data set. Since the core is elongated along the NE-SW (Figures 4, 5 and 9), we select the two cutting axes at P.A. of 45° and 135°, passing through the position of the 3 mm source as the major and minor axes, respectively. Along the major axis, the 45 m data show a weak velocity gradient from NE toward SW in both the molecular lines. The gradient along the major axis is an order of 1 km s⁻¹ pc⁻¹, comparable to the typical value measured in the Taurus dark cloud cores (Goodman et al. 1993). If the gradient represents the rigid-body-like rotation of the core, it is converted to an angular velocity of $\Lambda \simeq 3 \times 10^{-14} \ \rm s^{-1}$. On the other hand, the minor axis plots do not show a well-defined velocity gradient commonly seen in the two lines, although the H¹³CO⁺ diagram appears to show an SE-NW gradient if we concentrate on the lowest two contours.

Another important finding from Figure 12 is the presence of broader line width region at the core center, prominently seen for the $\rm H^{13}CO^{+}$. The blueshifted gas is seen up to $\simeq 0.6$ km s⁻¹ from the $V_{\rm sys}$ at the central region of $r \lesssim 5''$ (corresponding to 1000 AU), whereas the redshifted counterpart about $\simeq 0.3$ km s⁻¹. The presence of such blueshifted emission and the weak redshifted counterpart at the core center (see also Figure 2) suggests that gas

is infalling where redshifted gas is obscured by the foreground cold gas along the line-of-sight (e.g., Walker et al. 1986). Notice that the line broadening at the core center is unlikely to be caused by the possible compact outflow because the red lobe is more intense than the blue one (see Figure 8), inconsistent with the above results.

4.5.2. Velocity Width

We firstly estimate intrinsic velocity width ($\Delta v_{\rm int}$) toward the core center by analyzing the N₂H⁺, H¹³CO⁺, C₃H₂, CCS, and NH₃ lines (Table 5). Note that $\Delta v_{\rm int}$ is the velocity width corrected for line broadening due to instrumental velocity resolution and optical depth of the line (Phillips et al. 1979). Both corrections are made for the C₃H₂ and CCS lines. The latter correction is not made for N₂H⁺ and NH₃ data because HFS analysis obtains the optical-depth-free $\Delta v_{\rm FWHM}$ (see Appendix B), and not for the H¹³CO⁺ data because it is optically thin. The obtained $\Delta v_{\rm int}$ toward the center is between 0.35 and 0.61 km s⁻¹. This range is 2~3.5 times larger than the isothermal sound speed ($c_{\rm s}$) of the ambient gas of 0.18 km s⁻¹ at $T_{\rm k} = 9.5$ K (§4.1.1).

Subsequently, we analyzed velocity width structure of the core. Figure 13 shows the $\Delta v_{\rm int}$ maps made by spectral moment analysis of the 45 m telescope N₂H⁺ (1–0) F₁,F=0,1– 1,2 and H¹³CO⁺ (1–0) line data. We adopt the moment method to keep a consistency in the analysis between the two lines. To make the maps, we made spectra from the cube data at each point, then searched for a peak LSR-velocity in each spectrum to determine two velocity ranges from the peak velocity toward both the blue- and redshifted sides where the intensities are above the 1.5 σ level. We calculated the second-order spectral moments over the velocity ranges defined for the individual spectra. For the N₂H⁺ map (Figure 13b), we corrected the line broadening effect due to optical depth. We used Eq.(3) in Phillips et al. (1979) by substituting $\tau_{\rm p}$ of Eq.(3) with $\tau_{\rm tot} \times s$ where s is the intrinsic relative intensity of the $F_1, F = 0, 1-1, 2$ transition (0.111; Cazzoli et al. 1986). The maximum line broadening at the most opaque ($\tau_{\text{tot}} \times 0.111 = 1.5$) position is 1.3 times the width for $\tau_{\text{p}} \to 0$. Considering the thermal noise and the velocity resolutions, we estimate uncertainties of 0.11 and 0.12 km s⁻¹ in $\Delta v_{\rm int}$ for N₂H⁺ and H¹³CO⁺, respectively. As seen in PV diagrams (§4.5.1), both the N_2H^+ and $H^{13}CO^+$ maps show a clear increase of $\Delta v_{\rm int}$ toward the core center. The peak of the broadening does not fall onto the core center. It also should be noted that $\Delta v_{\rm int}$ of the core gas exceeds c_s of 0.18 km s⁻¹ over the core (see also Table 5). Furthermore, comparing Figures 8 and 13, one cannot discern any clear effects such as an evacuated shell by the possible compact outflow in Figure 8; the ¹²CO (3–2) condensations are only observed toward the 3 mm continuum source.

The above analysis clearly shows that there exist non-thermal motions in the core. We estimate non-thermal velocity width $(\Delta v_{\rm nth})$ by subtracting the thermal velocity width $(\Delta v_{\rm thm})$ from $\Delta v_{\rm int}$: $(\Delta v_{\rm int})^2 = (\Delta v_{\rm thm})^2 + (\Delta v_{\rm nth})^2$. Here the thermal contribution is given by $\Delta v_{\rm thm} = \sqrt{\frac{8(\ln 2)kT_k}{m_{\rm mol}}}$ where k is the Boltzmann constant, and $m_{\rm mol}$ is the molecular weight: 29 amu for N₂H⁺, 30 amu for H¹³CO⁺, 56 amu for CCS, and 17 amu for NH₃. Assuming that T_k is equal to $T_{\rm ex}$ of 9.5 K (§4.1.1) and that T_k is constant over the entire core, $\Delta v_{\rm thm}$ is calculated to be 0.12 km s⁻¹ for N₂H⁺, 0.12 km s⁻¹ for H¹³CO⁺, 0.09 km s⁻¹ for CCS, and 0.16 km s⁻¹ for NH₃ lines. This leads to mean non-thermal velocity widths over the core of $\langle \Delta v_{\rm nth} \rangle = 0.21$, 0.58, 0.40, and 0.46 km s⁻¹ for the N₂H⁺, H¹³CO⁺, CCS, and NH₃ lines, respectively, suggesting the presence of supersonic gas motions. In obtaining $\langle \Delta v_{\rm nth} \rangle$, we used the $\langle \Delta v_{\rm int} \rangle$ values in Table 5.

5. Discussion

5.1. Evolutionary Stage of the GF 9-2 Core: A Very Young Protostar Before Formation of a Large-Scale Molecular Outflow

With its low luminosity ($\simeq 0.3~L_{\odot}$) and cold SED ($T_{\rm bol} \leq 20~\rm K$; Wiesemeyer et al. 1997), we believe that the protostar embedded in GF 9-2 core is at an extremely early phase of low-mass star formation, evidenced by the absence of a large-scale high-velocity molecular outflow, the possible detection of a compact low-velocity outflow, and the detection of H₂O masers. We estimate the protostar's age from dynamical age ($t_{\rm dyn}$) of the possible compact low-velocity outflow (§3.3.1). The terminal velocity ($V_{\rm t}$) of the spectra would give the line-of-sight component of the outflow velocity of $|V_{\rm t} - V_{\rm sys}| = V_{\rm flow} \cos i$ where i is the inclination angle of the outflow axis to the line-of-sight. Given the projected lobe length of $l_{\rm lobe} \sin i = 1,1000$ and 6600 AU and $V_{\rm flow} \cos i \simeq 3.3$ and 3.1 km s⁻¹ (§3.3.1), we have $t_{\rm dyn} = l_{\rm lobe}/V_{\rm flow} \simeq 1.6 \times 10^4$ and 1.0×10^4 years with $i = 45^{\circ}$ for the blue- and redshifted ¹²CO (3–2) lobes, respectively. These dynamical ages are comparable to those for the extremely young class 0 sources, e.g., $(0.6-3)\times 10^4$ years for VLA 1623 and $(0.8-2)\times 10^4$ years for IRAM 04191 (Table 1 in André, Motte & Backman 1999, and references therein).

The youth of GF 9-2 is demonstrated in Figure 14 where we present a plot of CO outflow momentum rate $(F_{\rm CO})$ normalized by the bolometric luminosity $(F_{\rm CO} \cdot c/L_{\rm bol})$ vs. $T_{\rm bol}$ for nearby $(d \leq 350~{\rm pc})$ low-mass $(L_{\rm bol} \leq 50~L_{\odot})$ YSOs. We employ $F_{\rm CO} \cdot c/L_{\rm bol}$ because molecular outflows in low-mass protostars are likely to be momentum-driven (e.g., Cabrit & Bertout 1992; Richer et al. 2000, and references therein). The temperature $T_{\rm bol}$ is believed to trace the evolutionary stage of YSOs (Myers & Ladd 1993). We calculate 3σ

upper limit of $F_{\rm CO} \cdot c/L_{\rm bol} = \frac{M_{\rm lobe} V_{\rm flow}^2}{l_{\rm lobe}} \cdot \frac{c}{L_{\rm bol}} \simeq 9$ and 20 for the ¹²CO (3–2) blue- and red lobes, respectively, with $i=45^{\circ}$. Figure 14 illustrates that "class 0" is the most powerful outflow phase and "class I" is the decline phase (e.g., Moriarty-Schieven et al. 1994). The most remarkable result is that GF 9-2 shows the lowest outflow activity, among the coldest low-mass class 0 sources, although there exists enough circumstellar material (§4.3) to be dragged by a possible protostellar jet to develop a large-scale molecular outflow. Note that the prototypical class 0 sources of VLA 1623 (AWB93) and IRAM 04191 (André et al. 1999) have powerful CO outflows, despite that their bolometric luminosities are comparable to that of GF 9-2: 1 L_{\odot} for VLA 1623 and 0.15 L_{\odot} for IRAM 04191. We thus believe that the low luminosity of GF 9-2 is not responsible for the lowest outflow activity. Consequently, it is very likely that the protostar of our interest is the youngest class 0 protostar ever identified and is just at the beginning of the outflow launch.

5.2. The Initial Conditions for Gravitational Collapse of a Low-Mass Star Forming Core

5.2.1. Stability of the GF 9-2 Core

If we interpret that the non-thermal velocity width obtained in GF 9-2 core (§4.5.2) is attributed to turbulent motions, we expect that the turbulence can help support the core against its self-gravity. To test this hypothesis, we compare the LTE mass of the core with virial mass $M_{\rm vir}$ including the turbulence. Assuming a spherical system, the virial mass is given by $M_{\rm vir} \simeq R_{\rm eff} \langle \Delta v_{\rm int} \rangle^2 / G$ where $\langle \Delta v_{\rm int} \rangle$ includes the non-thermal width, i.e., the turbulence. Given $\langle \Delta v_{\rm int} \rangle$ and $R_{\rm eff}$ values (Tables 5 and 8), we found that $M_{\rm vir}$ ranges from 0.39 to 2.9 M_{\odot} (case I in Table 8). Since $M_{\rm vir} \simeq M_{\rm LTE}$ within the uncertainties, the core is most likely to be in virial equilibrium. However, it should be noted that this hypothesis does not reconcile with the line broadening toward the core center (Figure 13). Moreover, as far as we know, no cores which are supported by turbulence exhibit a $\rho(r) \propto r^{-2}$ density profiles (see Figure 11). Therefore, we conclude that the non-thermal line width is not caused by turbulence.

Alternatively, if we consider that infall causes the non-thermal line width, that is, if GF 9-2 core is gravitationally unstable, the drawbacks in the previous hypothesis would be solved. The presence of infalling motion is supported by the following facts: (1) the presence of the blueshifted gas and the less prominent redshifted counterpart in the central $r \leq 1000$ AU (§4.5.1), (2) the spectroscopic signature of infall, i.e., the "blue-skewed" profile observed in the optically thick N₂H⁺ (1–0) F₁,F=0,1–1,2 line (Figure 2), and (3) the detection of the H₂O masers, a clear signpost of star formation, naturally leading to the presence of

accretion flow onto the star-disk system. We, however, point out a drawback in the above (2); the optically thin H¹³CO⁺ emission does not show a single Gaussian profile expected from the infall interpretation, while the CCS does. In this interpretation, $M_{\rm vir}$ should be estimated only from the thermal motion as $M_{\rm vir} = \frac{R_{\rm eff}}{G} \frac{kT_{\rm k}}{\mu m_{\rm H}}$. The estimated $M_{\rm vir}$ from the 4 lines takes a range between 0.078 and 0.25 M_{\odot} (case II in Table 8) which is one order of magnitude smaller than $M_{\rm LTE}$. The small $M_{\rm vir}$ is consistent with our interpretation that the core is under gravitational collapse. As discussed in §4.5.2, the core would be rotating with $\Lambda \simeq 10^{-14}~{\rm s}^{-1}$. The collapse cannot be supposed by the centrifugal force due to the rotation because the rotational energy is less than a few percent of total energy required to support the core against its self-gravity. For such an unstable core, the gas is expected to be more perturbed toward the center, and the velocity width should increase inward as a result. In fact, Figure 13 clearly indicates that $\Delta v_{\rm int}$ in GF 9-2 increases up to $\simeq 0.6~{\rm km~s^{-1}}$ toward the center.

5.2.2. Initial Conditions for the Gravitational Collapse of the Core

To bring out the initial conditions for the gravitational collapse in GF 9-2 core, we examine the density and velocity structures by comparing with some key characteristics of the Shu (1977) and Larson-Penston (Larson 1969; Penston 1969) solutions. The radial H₂ column density profile of the core is given by $(7.7\pm4.1)\times10^{23}\left(\frac{\mathrm{X(N_2H^+)}}{9.5\times10^{-10}}\right)^{-1}\left(\frac{r}{200\mathrm{AU}}\right)^{-(1.0\pm0.1)}$ cm⁻² for $0.001<\frac{r}{\mathrm{pc}}<0.05$ from the combined data and $(8.9\pm4.5)\times10^{23}\left(\frac{\mathrm{X(N_2H^+)}}{9.5\times10^{-10}}\right)^{-1}\left(\frac{r}{200\mathrm{AU}}\right)^{-(1.1\pm0.2)}$ cm⁻² for $0.005<\frac{r}{\mathrm{pc}}<0.08$ from the 45 m data (Figure 11). It should be noted that the dense N₂H⁺ gas seem to obey the power-law profile with the index of -1 even at the innermost region of $r\lesssim1000$ AU where a possible compact outflow might begin to destroy the core. The power-law indices of -1.0 and -1.1, converted into -2.0 and -2.1 for the volume density, well agree with those in the two solutions after the formation of the protostar (Shu 1977; Whitworth & Summers 1985). The best-fit H₂ column densities at r=200 AU fall between the two extreme predictions at T=9.5 K: $(2.8\pm1.5)\times10^{23}$ cm⁻² for the Shu and $(13\pm7)\times10^{23}$ cm⁻² for the Larson-Penston solutions. Here we used a relation of $N_0(\mathrm{H}_2)=1.0$ and 1.0 cm⁻² for the Shu's and Larson-Penston's cases, respectively (Hunter 1977; Shu 1977; Foster & Chevalier 1993). Because of the abundance uncertainty, however, we cannot conclude which solution describes well the collapse in GF 9-2 core.

Contrary to the above discussion based on the density profile, the velocity width maps (Figure 13) help to discriminate the two theoretical scenarios for the collapse of GF 9-2 core. Notice that the influence of the compact outflow on the velocity width cannot be discerned

toward the 3 mm source. Figure 13 shows that the velocity width decreases outward, but remains $\simeq 0.3$ km s⁻¹, which is twice the ambient $c_{\rm s}$, even in the outermost region of $r \simeq 50''$ (corresponding to 0.05 pc) where the density profile shows $\rho(r) \propto r^{-2}$ (Figure 11). Recall that $\rho(r) \propto r^{-2}$ profile characterizes outer part of a collapsing core. These facts clearly indicate that the extended Larson-Penston solution for t > 0 is more likely to be the case because it requires the infalling state when a protostar is about to be born $(v(r) \sim -3.28c_{\rm s}$ at $t \to -0$; Hunter 1977), whereas the Shu solution requires a static state (v(r) = 0 at t = 0). It is, therefore, highly probable that the gravitational collapse of GF 9-2 core is well described by the runaway collapse scenario.

Subsequently, we estimate the age of the GF 9-2 protostar $(t_{\rm protostar})$ based on the lack of the density profile of $\rho(r) \propto r^{-3/2}$ down to the innermost region of $r \simeq 3''$ (see Figure 11). Recall that $\rho(r) \propto r^{-3/2}$ profile is expected for a central free-fall region which appears in both of the solutions at t > 0. The non-detection of a free-fall density profile indicates that the central free-fall region, propagating outward with supersonic velocity, has not yet developed up to a radius $(r_{\rm ff})$ of $\simeq 600$ AU, suggestive of the youth of the GF 9-2 protostar. However, we do not exclude the possibility that the absence of a detection of the $\rho(r) \propto r^{-3/2}$ profile at the center could be caused by the formation of binary (described in §5.3) whose projected separation is $\simeq 1200$ AU. Using Eqs. (9) and (10) in Ogino, Tomisaka & Nakamura (1999), we estimate $t_{\rm protostar}$ to be less than $t_{\rm protostar} \simeq 5000 \left(\frac{T}{9.5~\rm K}\right)^{-\frac{1}{2}}$ years since the formation of the central protostar for the Larson-Penston solution. Although the age estimate is a factor of 2–3 smaller than the outflow dynamical age of $t_{\rm dyn} \simeq (1.0-1.6) \times 10^4$ years (§5.1), we argue that the central protostar has just begun to exhibit its jet activity traced by the H₂O masers (§5.1).

Consequently, we propose that GF 9-2 core has started its gravitational collapse with initially unstable state. Here, the term *initial* means $t = -t_{\rm ff}$ where $t_{\rm ff}$ is free-fall time of the core (Larson 1969; Penston 1969). For GF 9-2, we calculate $t_{\rm ff} \simeq 2 \times 10^5$ years. We therefore believe that the age of the core, $t_{\rm core} = t_{\rm ff} + t_{\rm protostar}$, would be $\simeq 2 \times 10^5$ years, which has a consistency with the time scale of chemical evolution (§4.2.2).

5.2.3. Infall Velocity and Mass Accretion Rate in the Core

Assuming that $\Delta v_{\rm int}$ represents a velocity difference of blue- and redshifted infalling gas along the line-of-sight, let us discuss infall velocity $(v_{\rm inf})$ of the core gas. We found that $v_{\rm inf}$ varies from 0.2 to 0.4 km s⁻¹ using a relation of $v_{\rm inf} \simeq \frac{1}{2} |v_{\rm inf,red} - v_{\rm inf,blue}|/\cos i \simeq \frac{\Delta v_{\rm int}}{2\cos i}$ for the $\Delta v_{\rm int}$ range of (0.28 – 0.63) km s⁻¹ over the core (see Figure 15) and $i=45^{\circ}$. We now calculate the mass infall rate from $\frac{dM}{dt} = 4\pi R_{\rm eff}^2 \mu m_{\rm H} \cdot n_{\rm H_2}(R_{\rm eff}) \cdot v_{\rm inf} \simeq 2\pi R_{\rm eff} \cdot \frac{\mu m_{\rm H} \cdot N_{\rm N_2H^+}(R_{\rm eff})}{X(N_2H^+)}$.

 $v_{\rm inf}$ for a sphere with the radius of $R_{\rm eff}$. Here $n_{\rm H_2}(R_{\rm eff})$ is a volume density of a thin shell whose radius is $R_{\rm eff}$ and is approximated as $\frac{N_{\rm N_2H^+}(R_{\rm eff})}{2R_{\rm eff}\cdot X(N_2H^+)}$. Given $v_{\rm inf}=0.29~{\rm km~s^{-1}}$ at $r\simeq R_{\rm eff}$ from the N₂H⁺ $\Delta v_{\rm int}$ map (Figure 13), we have $\frac{dM}{dt}\simeq 3\times 10^{-5}~M_{\odot}$ year⁻¹ with uncertainty of a factor 1.6 for $R_{\rm eff}$ in Table 8, the column density profile (§4.4), and $X_{\rm m}$ in Table 7. The inferred mass accretion rate falls within the range between the predicted values of 1.5×10^{-6} and $7.4\times 10^{-5}~M_{\odot}$ year⁻¹ for the Shu and Larson-Penston solutions, respectively, at 10 K. These accretion rates are calculated by $m_0c_{\rm iso}^3/G$ where m_0 is the non-dimensional factor of 0.975 for the Shu and 46.92 for the Larson-Penston solutions (Hunter 1977). Our small mass accretion rate, compared to that of the Larson-Penston's solution, is attributed to both the smaller column density and infall velocity.

5.3. Is a Protobinary System Forming?

We found that the position of 3 mm continuum source is displaced by $\simeq 6''$ to the east of the N₂H⁺ column density peak, which would be explained by the presence of a protobinary system. In this interpretation, the 3 mm source represents a protostar and the N₂H⁺ peak a preprotostellar condensation. This is because the N₂H⁺ condensation is deeply embedded in the extended $350 \,\mu\mathrm{m}$ emission (Figure 9b), but is not accompanied with a compact $3 \,\mathrm{mm}$ source. To investigate the nature of the binary members, we made a $\Delta v_{\rm int}$ map from the combined H¹³CO⁺ data shown in Figure 15 as the line is expected to be optically thin. In §3.1.2, we asserted that the 3 mm continuum emission would represent circumstellar material around a protostar. The line broadening toward the 3 mm source seen in Figures 12 and 15 suggests the local enhancement of mass accretion, leading to the existence of a protostar. On the other hand, the N₂H⁺ peak (white contour) seems to be a gas condensation or a preprotostellar core rather than an apparent peak caused by local abundance enhancement because $X(N_2H^+)_{s''}$ inferred over the 3σ level contour of $350\,\mu\mathrm{m}$ emission is comparable to those obtained with low spatial-resolution studies (§4.2.1). It should be noted that the H¹³CO⁺ emission has a secondary peak near the N₂H⁺ condensation as seen in the OVRO maps (Figure 6). Furthermore, the combined N₂H⁺ map (Figure 6) does not show a shelllike structure which is expected to be seen if N₂H⁺ disappears from the gas phase at the core center (e.g., Kuiper, Velusamy & Langer 1996; Belloche & André 2004). We therefore conclude that the positional displacement of N₂H⁺ peak is not caused by chemical evolution, but the N₂H⁺ peak represents a preprotostellar condensation, making it younger than the eastern object. The detection of the two objects reinforces the assertion that we witness a forming binary system with a separation of $\simeq 1200$ AU.

The masses of the circumstellar material $(M_{\rm cm})$ for each binary member would be an

order of 0.1 M_{\odot} . For the eastern object, the 3 mm continuum flux density (§3.1.2) integrated inside its 3σ level contour (see Figure 15) implies that the gas plus dust mass ranges from $\simeq 0.1$ (case I in §3.1.2) to 0.2 M_{\odot} (case II). For the western object, we estimate (0.1-0.3) M_{\odot} from the N₂H⁺ intensity integrated inside the white contour, whose extent is similar to that of the 3 mm source (Figure 15). The inferred $M_{\rm cm}$ seem reasonable for an amount of circumstellar material with 100 AU scale around a newly formed protostar at the very early accretion phase because of $M_{\rm cm} \simeq M_{\rm protostar} = \frac{dM}{dt} \times t_{\rm protostar} \simeq 0.15~M_{\odot}$ (§5.2.2 and 5.2.3). In this context, the EW elongated structure at the core center seen in the 45 m maps (Figure 6) may be interpreted as a 1000 AU scale circumbinary disk-like structure because the size would be smaller than the extent of the protostellar envelope traced by the $350 \,\mu\mathrm{m}$ continuum emission (6600×4500 AU; §3.1.2). It is impossible to uniquely define spatial extent of the disk-like structure. However, if we arbitrarily define the disk-like structure by a region enclosed by the 18 or 21σ level contours of the combined H¹³CO⁺ map (Figure 15), mass of the circumbinary disk-like structure $(M_{\rm cbd})$ calculated from the N_2H^+ data would range $(0.2-0.5)~M_{\odot}$ with an approximate effective radius of $\simeq 2000$ AU. Considering the uncertainties in spatial extents and in κ_0 , β (§3.1.2) and X(N₂H⁺) (§4.2.1), the mass of disklike structure is likely to be plausible to be hosted in the $(0.4-0.8)~M_{\odot}$ envelope (§3.1.2) and to host the two binary members with the 0.1 M_{\odot} order circumstellar material. The mass distribution of $M_{\rm core} > M_{\rm env} \gtrsim M_{\rm cbd} \gtrsim M_{\rm cm}$ does not contradict with our hypothesis that the central protostar(s) is at extremely early evolutionary phase.

If a circumbinary disk exists, the radius of disk-like structure would be physically related to the rotation of the natal core, described in §4.5.1. Although the axis for the large-scale rotation of the core (P.A. $\simeq 135^{\circ}$) is not perpendicular to the major axis of the disk-like structure (P.A. $\simeq 90^{\circ}$), a rough estimate of radius of the disk-like structure would be given by the centrifugal radius, R_{cent} , calculated from the specific angular moment of the core gas. With a relation of $R_{\rm cent} = (4R_{\rm eff}^4\Lambda^2)/(GM_{\rm cbd})$, we obtained $R_{\rm cent} \simeq 900$ AU for Λ of $3 \times 10^{-14} \text{ s}^{-1}$ (§4.5.1) and R_{eff} in Table 8. The centrifugal radius is roughly twice the radius of disk-like structure, probably supporting our interpretation. Lastly, let us estimate the Toomre's Q parameter to examine whether or not gravitational fragmentation of the disk-like structure led to the formation of the binary. The Q parameter is given by $\frac{\Lambda c_s}{\pi G \Sigma}$ for Keplerian rotation. Here Σ is the surface density of the disk-like structure given by $M_{\rm cbd}/A_{\rm cbd}$; an area of $\mathcal{A}_{\rm cbd} \simeq 4 \times 10^{33} \ {\rm cm}^2$ is calculated for the region described above. We obtained $Q \simeq 0.01 \left(\frac{\Lambda}{3\times 10^{-14} \ {\rm s}^{-1}}\right) \left(\frac{T}{10 \ {\rm K}}\right)^{\frac{1}{2}} \left(\frac{M_{\rm cbd}}{0.4M_{\odot}}\right)^{-1} \left(\frac{\mathcal{A}_{\rm cbd}}{4\times 10^{33} \ {\rm cm}^2}\right)$. Considering the uncertainties in the input parameters, it is certain that the Q value is less than unity. We, therefore, suggest that the binary system is likely to be forming in the core center due to the gravitational fragmentation of the circumbinary disk-like structure, whose radius appears to be determined by the rotation of the core.

6. Summary and Future Works

The main findings of this work and future considerations are summarized as follows.

- 1. Our high density gas observations identified a molecular cloud core with a size of \simeq 0.08 pc toward GF 9-2. In the core center, a protostellar envelope with a size of \simeq 4500 AU is identified through 350 μ m continuum emission. The mass of the core and the envelope are \simeq 3 and \simeq 0.6 M_{\odot} , respectively. Obtaining fractional abundances of the probe molecules, we propose that GF 9-2 core should be at an early phase of chemical evolution, although the radial variations of the abundances should be revealed to accurately assess the chemical evolutionary stage.
- 2. Our deep search for CO wing emission revealed that the protostar in GF 9-2 has not developed a large-scale high-velocity "jet-like" outflow. Instead, a compact low-velocity outflow may be formed at the core center. Thus, GF 9-2 is very likely to be at an extremely early stage in low-mass star formation before arriving its most active outflow phase. To test the conclusion, we need to conduct high angular resolution and deeper search for compact outflow(s) in higher-J transitions of CO.
- 3. The radial column density profile of the core can be well fitted by a power-law form of $\rho(r) \propto r^{-2}$ for 0.003 < r/pc < 0.08 region. The power-law index of -2 agrees with the expectation for an outer part of gravitationally collapsing core. On the other hand, based on the absence of a $\rho(r) \propto r^{-3/2}$ profile, we found that a central free-fall region has not developed in a region larger than $r \simeq 600$ AU.
- 4. The PV analysis identified a large-scale velocity gradient with an order of 1 km s⁻¹ pc⁻¹ along the major axis of the core. The gradient is interpreted as a rigid-body-like rotation with an angular velocity of $\simeq 3 \times 10^{-14}$ s⁻¹, comparable to those measured in other similar cores. We found that the gas is supersonic all over the core and that the velocity width is enhanced up to $\simeq 0.6$ km s⁻¹ in the central 1000 AU toward the 3 mm source. The supersonic velocity width and the $\rho(r) \propto r^{-2}$ profile are explained by infall in the extension of the runaway collapse scenario proposed by Larson and Penston for t > 0. The current mass accretion rate of $\simeq 3 \times 10^{-5}$ M_{\odot} year⁻¹ is estimated from $v_{\rm inf} \simeq 0.3$ km s⁻¹ at $r \simeq 7000$ AU. We discuss the likelihood that GF 9-2 core has been undergoing gravitational collapse $\lesssim 5000$ years, starting from initially unstable conditions.
- 5. We discovered a potential protobinary system with a projected separation of $\simeq 1200$ AU embedded in a circumbinary disk-like structure with $\simeq 2000$ AU radius at the core

center. The binary consists of a very young protostar and a preprotostellar condensation. The circumbinary material mass is on the order of $0.1 M_{\odot}$. Taking account of the centrifugal radius calculated from the core rotation and the Toomre's Q value for the disk, we suggest that the binary formation may have been initiated by gravitational fragmentation of the circumbinary disk-like structure. Further studies are needed using high-angular-resolution deep imaging in submm and FIR continuum emission.

The authors sincerely acknowledge an anonymous referee whose comments significantly improved the quality of the paper. R.S.F. acknowledges A. I. Sargent and J. M. Carpenter for critical readings of the manuscript and continuous encouragement. The authors thank H. Yoshida for providing the telescope time at CSO to obtain the ¹²CO (3–2) data, S. Takakuwa, J. Lamb, D. Woody, K. Sunada, and S. Okumura for fruitful discussion about data combining of single-dish telescope and interferometer, H. Wiesemeyer for information on GF 9-2 including the distance and the luminosity, and L. Testi for his early contribution to this study. R. S. F. also appreciates discussion with A. Wootten, R. Cesaroni, E. van Dishoeck, H. Butner, G. Blake, T. Hanawa, T. Matsumoto, Y. Aikawa, K. Tachihara, T. Velusamy, and D. Ward-Thompson. R. S. F. and H. S. thank M. Yang, A. Kovácas, C. Borys and A. C. A. Boogert for their support at the SHARC II observations and data reduction. The authors gratefully acknowledge all the staff at OVRO, NRO, CSO, VLA, and the GILDAS software group at IRAM. Research at the Owens Valley Radio Observatory is supported by the National Science Foundation through NSF grant AST 02-28955.

A. Combining the OVRO mm-array and Nobeyama 45 m Telescope Data

We describe a method of combining the OVRO mm-array and Nobeyama 45 m telescope data to obtain high-spatial-resolution and missing-flux free images. We used the 45 m data to fill the central u-v hole of the mm-array visibility data. Since the OVRO array consists of six 10.4 m diameter telescopes, we can attain the minimum projected baseline length normalized by the observing wavelength $(D_{\lambda,\text{int}}^{\text{min}})$ of $\simeq 3.5~k\lambda$ at 3 mm when the array takes the most compact "C" configuration. The minimum spatial frequency is sufficiently smaller than the maximum spatial frequency of $D_{\lambda \text{SD}}^{\text{N}} = 15~k\lambda$ for a spatially Nyquist sampled 45 m telescope map. Therefore, the usage of the 45 m maps works to recover the flux densities missed by the mm-array. The basics of the data combination are described in Vogel et al. (1984), and our method here is similar to those in the previous works (e.g., Takakuwa et al. 2003). We took the following steps to make the combined maps.

- 1. For the BEARS H¹³CO⁺ data, we used the spectra taken with the inner 9 beams centered on the central beam on axis. The alignment of the 9 beams can be approximated as a regular grid with 41".4 spacing for our RMS pointing accuracy of $\lesssim 2$ ". This makes the resultant map grid spacing of 20".7, i.e., full-beam sampling. Obtaining the data on a regular grid is required to use Fast Fourier Transformation (FFT). As for the N₂H⁺, we used the data on a regular grid of 17" spacing (full-beam sampling) with pointing accuracy of $\lesssim 2$ ". To achieve the excellent pointing accuracy, we used the spectra under wind speeds of $\lesssim 2 \text{ m s}^{-1}$. We corrected the $T_{\rm mb}$ scale of the H¹³CO⁺ data with the BEARS in double sideband mode by observing the core center with the S80/S100 receivers having single sideband filters. Since $T_{\rm mb}$ at the core center is 0.73±0.04 K by the S80/S100 receivers with 18".5 beam and 0.91±0.1 K by the BEARS with 20".3 beam, we scaled the intensities of the BEARS data by a factor of 0.80.
- 2. To have a common frequency resolution between the OVRO and $45 \,\mathrm{m}$ telescope data, the $45 \,\mathrm{m}$ N₂H⁺ spectra, which have a 37 kHz spectral resolution, are smoothed in the same frequency bins as those of the OVRO data with a 125 kHz resolution. For the H¹³CO⁺ line, the $45 \,\mathrm{m}$ and OVRO data have the same frequency bins.
- 3. We made the $45\,\mathrm{m}$ maps by full-beam sampling on the regular grids with spacings of $20\rlap.{''}7~(=41\rlap.{''}4/2)$ for $\mathrm{H^{13}CO^{+}}$ and $17\rlap.{''}0$ for $\mathrm{N_2H^{+}}$. We did not apply the task BPOSC in the NEWSTAR package, which corrects the misalignment between the 25 beams on the sky plane, to the $\mathrm{H^{13}CO^{+}}$ data. Note that our OVRO field of view (FoV) with a single pointing does not cover the whole extent of the core.
- 4. In converting the $T_{\rm mb}$ scale of the 45 m maps into the flux density per beam solid angle (F_{ν}) , we calculated conversion factors through a relation of $F_{\nu} = I_{\nu}\Omega_{\rm beam}$ with the Rayleigh-Jeans approximation. Here I_{ν} is the specific intensity and $\Omega_{\rm beam}$ is the beam solid angle. The conversion factors are given by $\frac{F_{\nu}}{T_{\rm mb}} = \frac{2k}{\lambda^2} \cdot \frac{\pi \theta_{\rm HPBW}^2}{4 \ln 2} = 3.27 \left(\frac{3 \text{ mm}}{\lambda}\right)^2 \left(\frac{\theta_{\rm HPBW}}{20''}\right)^2$ (Jy beam⁻¹ K⁻¹).
- 5. To deconvolve the 45 m maps with its beam, the beam pattern is approximated by an axisymmetric Gaussian profile with HPBW of 20″.3 at 86.754 GHz for the BEARS H¹³CO⁺ data and 17″.2 at 93.173 GHz for the S80/S100 N₂H⁺ data. We adopt a mean HPBW of the inner 9 beams for BEARS (20″.3 ± 0″.3) H¹³CO⁺ observations. Note that the S80/S100 receivers have nearly equal beam pattern as they detect two independent linearly polarized waves by sharing common dewar and waveguide.
- 6. The 45 m maps are deconvolved by the Gaussian beams defined in (5). Since our 45 m maps satisfy the criteria discussed in Vogel et al. (1984), the deconvolution is done

by dividing the maps by the beam pattern. After several trials including the steps described below, the most plausible combined maps are obtained when the cut-off level of deconvolution is set to be 20% of the RMS noise level of the single-dish map so as not to miss high spatial frequency components having low amplitudes.

- 7. The deconvolved 45 m maps are convolved with the primary beam pattern of the OVRO 10.4 m antennas, assuming that all the six element telescopes have an axisymmetric Gaussian profile with HPBWs of 69.7 at 93.174 GHz and 75.0 at 86.754 GHz.
- 8. The single-dish maps are converted into visibility data in the u-v domain by FFT. As demonstrated in Figure 16, the visibility amplitudes from the two instruments agree well with each other over the common u-v distances. We stress that we did not apply amplitude scale corrections to both the 45 m and OVRO data.
- 9. The FFTed single-dish visibilities are used to make model visibilities which have the same integration time as the OVRO data (205 sec). Since our 45 m maps are sampled with the full-beam spacing, $\theta_{\text{SD}}^{\text{F}}$, we made model visibilities between zero and $D_{\lambda \text{SD}}^{\text{F}} = 1/(2\theta_{\text{SD}}^{\text{F}})$ on the basis of the sampling theorem. We calculated $D_{\lambda \text{SD}}^{\text{F}} = 6.10$ and 5.08 $k\lambda$ for the N₂H⁺ and H¹³CO⁺ data, respectively, and conservatively adopted smaller cut-off values of 5.3 and 4.5 $k\lambda$ to fill the central u-v holes in the OVRO data (Table 3).
- 10. We combined the 45 m and OVRO visibilities in the u-v plane, assuming that the 45 m model visibilities have a Gaussian distribution within a radius of $D_{\lambda \, \rm SD}^{\rm F}$ in the u-v plane. We found that synthesized beams of the combined maps are controlled by the visibility weighting function, regardless of the distribution of single-dish model visibilities.
- 11. To construct an image from the combined visibilities, we used the task IMAGR in the AIPS package where one can optimize the synthesized beam size and sensitivity of the resultant image by changing the robustness power of the weighting function. Figure 17 represents how the parameter affects the synthesized beam pattern and the dirty map (map affected by the side lobe pattern of the synthesize beam). Considering the trade-off between the beam size and the smoothness of the map, we selected the robustness power of −1 and CLEANed the dirty maps. We stopped the CLEAN loop before encountering the first negative CLEAN component because we are unable to find emission-free regions to estimate an RMS noise level, i.e., a threshold flux density to stop the loop, due to the extent of the core than the OVRO FoV.

B. Calculation of Column Density

To estimate the total column density of molecular gas (N_{tot}) through observations of the rotational transition from the upper J+1 to lower J level, we use the previously derived equation (e.g., Scoville et al. 1986) which gives N_{tot} through the optical depth (τ_v) and excitation temperature (T_{ex}) of the probe molecule as follows,

$$N_{\text{tot}} = \frac{3k}{8\pi^3 \mu^2 B} \cdot \frac{\left(T_{\text{ex}} + \frac{hB}{3k}\right)}{J+1} \cdot \frac{\exp\left\{\frac{hBJ(J+1)}{kT_{\text{ex}}}\right\}}{1 - \exp\left(-\frac{h\nu}{kT_{\text{ex}}}\right)} \int \tau_v dv$$
 (B1)

where k denotes the Boltzmann constant, h the Planck constant, μ the permanent dipole moment of the molecule, and B rotational constant, respectively. We should keep in mind that, to derive Eq.(B1), one has approximated the rotational partition function $Q(T_{\rm ex})$ as,

$$Q(T_{\rm ex}) \simeq \frac{k}{hB} \left\{ T_{\rm ex} + \frac{hB}{3k} \right\}.$$
 (B2)

B.1.
$$N_2H^+$$

To apply Eq.(B1) to the N₂H⁺ line data, we have to find $T_{\rm ex}$ and τ_{ν} . In the following, we describe how they are obtained from the N₂H⁺ spectra through the hyperfine structure (HFS) analysis. In local thermodynamic equilibrium (LTE), an observed brightness temperature ($T_{\rm b}$) is expressed by the following radiative transfer equation,

$$T_{\rm b} = f \cdot [J_{\nu}(T_{\rm ex}) - J_{\nu}(T_{\rm bg})] \{1 - e^{-\tau_{\nu}}\},$$
 (B3)

where $T_{\rm b}$ is replaced by the brightness temperatures averaged over a main beam $(T_{\rm mb})$ for single-dish observations, and over a synthesized beam $(T_{\rm sb})$ for interferometric observations. Here f denotes a beam filling factor, and $J_{\nu}(T)$ the equivalent Rayleigh-Jeans temperature given by $J_{\nu}(T) = \frac{h\nu}{k} \left\{ \exp\left(\frac{h\nu}{kT}\right) - 1 \right\}^{-1}$. From Eq.(B3), we fit the function of $y(v) = C\left[1 - \exp\left\{-\tau(v)\right\}\right]$ with a constant C to each N₂H⁺ hyperfine (HF) component. The optical depth is given by,

$$\tau(v) = \tau_{\text{tot}} \sum_{i=1}^{7} s_i \exp\left[-\frac{\{v - (V_{\text{sys}} + \delta v_i)\}^2}{2\sigma_i^2}\right],$$
 (B4)

as a function of velocity. Here $\tau_{\rm tot}$ denotes the total optical depth, i.e., a sum of the optical depths at the centers of the HF components, s_i the normalized relative intensity of the *i*th HF component taken from Cazzoli et al. (1985), δv_i the velocity offset of the *i*th component, and $\sigma_i^2 = \frac{(\Delta v_{\rm FWHM},i)^2}{8 \ln 2}$ with the velocity width in FWHM of the *i*th component $(\Delta v_{\rm FWHM},i)$. We assumed that the line broadening due to the thermal and non-thermal gas motions equally work for all the HF components since they are emanated from the same molecular ion in the same region. We thus simplified Eq. (B4) by adopting $\sigma_i = \sigma$ and $\Delta v_{\rm FWHM},i = \Delta v_{\rm FWHM}$. Therefore, the HFS analysis gives $\tau_{\rm tot}$, the center velocity $(V_{\rm sys} + \delta v_i)$, the velocity width $(\Delta v_{\rm FWHM})$, and the constant C. Since $C = f\{J_{\nu}(T_{\rm ex}) - J_{\nu}(T_{\rm bg})\}$, one can calculate $T_{\rm ex}$ by,

$$T_{\rm ex} = \frac{h\nu_0}{k} \left[\ln \left\{ 1 + \frac{h\nu_0}{k \left(C + J_{\nu} \left(T_{\rm bg} \right) \right)} \right\} \right]^{-1}.$$
 (B5)

Here we assumed f = 1.0 because the region of our interest is larger than the beam sizes. We now have the estimates of $T_{\rm ex}$, $\tau_{\rm tot}$, and $\Delta v_{\rm int}$ at each observing point (each pixel for the combined data). Since the integral in Eq.(B1) becomes

$$\int \tau_v dv = \frac{1}{2} \sqrt{\frac{\pi}{\ln 2}} \sum_{i=1}^{7} \tau_i \Delta v_{\text{int}} = \frac{1}{2} \sqrt{\frac{\pi}{\ln 2}} \cdot \tau_{\text{tot}} \Delta v_{\text{int}}, \tag{B6}$$

we have the desired expression to calculate the column density of N_2H^+ ($N_{N_2H^+}$) as follows,

$$N_{\rm N_2H^+} = 3.30 \times 10^{11} \frac{(T_{\rm ex} + 0.75)}{1 - e^{-4.47/T_{\rm ex}}} \left(\frac{\tau_{\rm tot}}{1.0}\right) \left(\frac{\Delta v_{\rm int}}{1.0 \text{ km s}^{-1}}\right) \text{ (cm}^{-2}).$$
 (B7)

Here we used $\mu=3.4$ D (Havenith et al. 1990) and B=46586.702 MHz (Caselli, Myers & Thaddeus 1995).

B.2. $H^{13}CO^{+}$

We estimated the column density of H¹³CO⁺ ($N_{\rm H^{13}CO^+}$) with Eq.(B1) giving the mean $T_{\rm ex}$ and τ_{ν_0} over the full extent of the core (Table 5) where τ_{ν_0} is a mean optical depth at the line center frequency of ν_0 . Since the radiative transfer equation of Eq.(B3) is written as $T_{\rm b} = f \cdot [J_{\nu}(T_{\rm ex}) - J_{\nu}(T_{\rm bg})] \cdot \tau_{\nu} \frac{(1-e^{-\tau_{\nu}})}{\tau_{\nu}}$, the integral of τ_{ν} can be expressed as,

$$\int \tau_{\nu}(v) \, dv \simeq \frac{\tau_{\nu_0}}{1 - e^{-\tau_{\nu_0}}} \cdot \frac{\int T_{\rm b}(v) \, dv}{J_{\nu}(T_{\rm ex}) - J_{\nu}(T_{\rm bg})} \quad \text{for } \tau_{\nu} \simeq 0.$$
 (B8)

Recall that $H^{13}CO^{+}$ (1–0) in GF 9-2 is optically thin (§4.1.2) and we assumed f = 1 in §B.1. Combining Eqs.(B1) and (B8), we obtain an expression to estimate the $H^{13}CO^{+}$ column density from single-dish data as,

$$N_{\rm H^{13}CO^{+}} = 2.32 \times 10^{11} \frac{(T_{\rm ex} + 0.69)}{1 - e^{-4.16/T_{\rm ex}}} \cdot \frac{1}{J_{\nu}(T_{\rm ex}) - J_{\nu}(T_{\rm bg})} \cdot \left(\frac{\int T_{\rm mb} dv}{1.0 \text{ K kms}^{-1}}\right) \text{ (cm}^{-2}).$$
 (B9)

Here we took $\mu = 4.07$ D (Haese & Woods 1979) and B = 43377.17 MHz. To have a complementary expression for interferometric data, we converted the flux density (F_{ν}) per synthesized beam into a brightness temperature per beam $(T_{\rm sb})$ through $T_{\rm sb} = \frac{\lambda^2}{2k\Omega_{\rm b}} \cdot F_{\nu}$ where $\Omega_{\rm b}$ is a beam solid angle given by $\frac{\pi}{4 \ln 2} (\theta_{\rm maj} \times \theta_{\rm min})$. Therefore, we have

$$N_{\rm H^{13}CO^{+}} = 3.77 \times 10^{13} \frac{(T_{\rm ex} + 0.69)}{1 - e^{-4.16/T_{\rm ex}}} \cdot \frac{1}{J_{\nu}(T_{\rm ex}) - J_{\nu}(T_{\rm bg})} \cdot \left(\frac{\Omega_{\rm b}}{1'' \times 1''}\right)^{-1} \left(\frac{\int F_{\nu} dv}{1.0 \text{ Jy kms}^{-1}}\right) \text{ (cm}^{-2}).$$
(B10)

B.3. CCS

Column density analysis of the CCS 4_3-3_2 line is similar with that for the H¹³CO⁺ line in the sense that we have only the representative values of $T_{\rm ex}$ and τ_{ν_0} over the entire core (Table 5). The observed CCS brightness temperature are converted into the column density through

$$N_{\rm CCS} = 8.16 \times 10^{11} \frac{(T_{\rm ex} + 0.73) \exp\left(\frac{3.73}{T_{\rm ex}}\right)}{1 - e^{-2.18/T_{\rm ex}}} \cdot \frac{\tau_{\nu_0}}{1 - e^{-\tau_{\nu_0}}} \cdot \frac{1}{J_{\nu}(T_{\rm ex}) - J_{\nu}(T_{\rm bg})} \cdot \left(\frac{\int T_{\rm mb} dv}{1.0 \text{ K kms}^{-1}}\right) \text{ (cm}^{-2}).$$
(B11)

Here we used $\mu = 2.81$ D (Murakami 1990), and B = 6477.75036 MHz (Yamamoto et al. 1990). Although the rotational energy (E_r) of the CCS molecule is given by $E_r = hBJ(J+1) - hDJ^2(J+1)^2$ considering the centrifugal stretching with D = 1727.96 kHz (Yamamoto et al. 1990), we ignored the D term to use the rotational partition function of Eq.(B2).

REFERENCES

Aikawa, Y., Ohashi, N., Inutsuka, S., Herbst, E., & Takakuwa, S. 2001, ApJ, 552, 639

André, P., Martin-Pintado, J., Despois, D., & Montmerle, T. 1990, A&A, 236, 180

André, P., Ward-Thompson, D., & Barsony, M. 1993, ApJ, 406, 122 (AWB93)

André, P., Ward-Thompson, D., & Motte, F. 1996, A&A, 314, 625

André, P., Motte, F., & Bacmann, A. 1999, ApJ, 513, L57

André, P., Ward-Thompson, D., & Barsony, M. 2000, Protostars and Planets IV, 59 (AWB00)

Bachiller, R. 1996, ARA&A, 34, 111

Beckwith, S. V. W., Henning, T., & Nakagawa, Y. 2000, Protostars and Planets IV, 533

Belloche, A., & André, P. 2004, A&A, 419, L35

Benson, P. J., Caselli, P., & Myers, P. C. 1998, ApJ, 506, 743

Bergin, E. A. & Langer, W. D. 1997, ApJ, 486, 316

Butner, H. M., Lada, E. A., & Loren, R. B. 1995, ApJ, 448, 207

Cabrit, S., & Bertout, C. 1992, A&A, 261, 274

Caselli, P., Myers, P. C., & Thaddeus, P. 1995, ApJ, 455, L77

Caselli, P., Benson, P. J., Myers, P. C., & Tafalla, M. 2002, ApJ, 572, 238

Claussen, M. J., Marvel, K. B., Wootten, A., & Wilking, B. A. 1998, ApJ, 507, L79

Chen, H., Myers, P. C., Ladd, E. F., & Wood, D. O. S. 1995, ApJ, 445, 377

Chernin, L. M. 1995, ApJ, 440, L97

Codella, C., Bachiller, R., & Reipurth, B. 1999, A&A, 343, 585

Cox, P., Walmsley, C. M., & Gusten, R. 1989, A&A, 209, 382

Dickman, R. L. 1978, ApJS, 37, 407

Dowell, C. D., et al. 2003, Proc. SPIE, 4855, 73

- Foster, P. N., & Chevalier, R. A. 1993, ApJ, 416, 303
- Furuya, R. S., Kitamura, Y., Saito, M., Kawabe, R., & Wootten, H. A. 1999, ApJ, 525, 821
- Furuya, R. S., Kitamura, Y., Wootten, H. A., Claussen, M. J., Saito, M., Marvel, K. B., & Kawabe, R. 2000, ApJ, 542, L135
- Furuya, R. S., Kitamura, Y., Wootten, H. A., Claussen, M. J., & Kawabe, R. 2001, ApJ, 559, L143
- Furuya, R. S., Kitamura, Y., Wootten, A., Claussen, M. J., & Kawabe, R. 2003, ApJS, 144, 71
- Goodman, A. A., Benson, P. J., Fuller, G. A., & Myers, P. C. 1993, ApJ, 406, 528
- Haese, N. N., & Woods, R. C. 1979, J. Chem. Phys., L61, 396
- Havenith, M., Zwart, E., Leo Meerts, W., & Ter Meulen, J. J. 1990, J. Chem. Phys., 93, 8446
- Ho, P. T. P. & Townes, C. H. 1983, ARA&A, 21, 239
- Hunter, C. 1977, ApJ, 218, 834
- Jijina, J., Myers, P. C., & Adams, F. C. 1999, ApJS, 125, 161
- Kovács, A. 2006, SHARC-2 $350 \,\mu\mathrm{m}$ Observations of Distant Submillimeter Galaxies and Techniques for the Optimal Analysis and Observing Weak Signals, Ph.D. Dissertation, California Institute of Technology
- Lai, S.-P., & Crutcher, R. M. 2000, ApJS, 128, 271
- Larson, R. B. 1969, MNRAS, 145, 271
- Leong, M. M. 2005, URSI Conf. Sec. J3-10, 426
- Mizuno, A., Onishi, T., Hayashi, M., Ohashi, N., Sunada, K., Hasegawa, T., & Fukui, Y. 1994, Nature, 368, 719
- Moriarty-Schieven, G. H., Wannier, P. G., Keene, J., & Tamura, M. 1994, ApJ, 436, 800
- Moscadelli, L., Testi, L., Furuya, R. S., Goddi, C., Claussen, M., Kitamura, Y., & Wootten, A. 2006, A&A, 446, 985
- Mundy, L. G., Looney, L. W., & Welch, W. J. 2000, Protostars and Planets IV, 355

Murakami, A. 1990, ApJ, 357, 288

Myers, P. C., & Benson, P. J. 1983, ApJ, 266, 309

Myers, P. C., & Ladd, E. F. 1993, ApJ, 413, L47

Ogino, S., Tomisaka, K., & Nakamura, F. 1999, PASJ, 51, 637

Ossenkopf, V., & Henning, T. 1994, A&A, 291, 943

Penston, M. V. 1969, MNRAS, 144, 425

Phillips, T. G., Wannier, P. G., Scoville, N. Z., & Huggins, P. J. 1979, ApJ, 231, 720

Preibisch, T., Ossenkopf, V., Yorke, H. W., & Henning, T. 1993, A&A, 279, 577

Richer, J. S., Padman, R., Ward-Thompson, D., Hills, R. E., & Harris, A. I. 1993, MNRAS, 262, 839

Richer, J. S., Shepherd, D. S., Cabrit, S., Bachiller, R., & Churchwell, E. 2000, Protostars and Planets IV, 867

Schilke, P., Walmsley, C. M., Pineau des Forets, G., & Flower, D. R. 1997, A&A, 321, 293

Schneider, S., & Elmegreen, B. G. 1979, ApJS, 41, 87

Scoville, N. Z., Sargent, A. I., Sanders, D. B., Claussen, M. J., Masson, C. R., Lo, K. Y., & Phillips, T. G. 1986, ApJ, 303, 416

Shinnaga, H., Ohashi, N., Lee, S., & Moriarty-Schieven, G. H. 2004, ApJ, 601, 962

Shu, F. H. 1977, ApJ, 214, 488

Shu, F. H., Adams, F. C., & Lizano, S. 1987, ARA&A, 25, 23

Stutzki, J., Ungerechts, H., & Winnewisser, G. 1982, A&A, 111, 201

Suzuki, H., Yamamoto, S., Ohishi, M., Kaifu, N., Ishikawa, S., Hirahara, Y., & Takano, S. 1992, ApJ, 392, 551

Tafalla, M., Myers, P. C., Caselli, P., Walmsley, C. M., & Comito, C. 2002, ApJ, 569, 815

Tafalla, M., Myers, P. C., Caselli, P., & Walmsley, C. M. 2004, A&A, 416, 191

Terebey, S., Vogel, S. N., & Myers, P. C. 1992, ApJ, 390, 181

Takakuwa, S., Kamazaki, T., Saito, M., & Hirano, N. 2003, ApJ, 584, 818

Ungerechts, H., Walmsley, C. M., & Winnewisser, G. 1980, A&A, 88, 259

Vogel, S. N., Wright, M. C. H., Plambeck, R. L., & Welch, W. J. 1984, ApJ, 283, 655

Yamamoto, S., et al., 1990, ApJ, 361, 318

Walker, C. K., Lada, C. J., Young, E. T., Maloney, P. R., & Wilking, B. A. 1986, ApJ, 309, L47

Ward-Thompson, D., Scott, P. F., Hills, R. E., & Andre, P. 1994, MNRAS, 268, 276

Whitworth, A., & Summers, D. 1985, MNRAS, 214, 1

Wiesemeyer, H. 1997, The spectral signature of accretion in low-mass protostars, Ph.D. Dissertation, University of Bonn

Wiesemeyer, H., Cox, P., Güsten, R., & Zylka, R. 1999, ESA SP-427: The Universe as Seen by ISO, 533

Winnewisser, G., Churchwell, E., & Walmsley, C. M. 1979, A&A, 72, 215

Wolkovitch, D., Langer, W. D., Goldsmith, P. F., & Heyer, M. 1997, ApJ, 477, 241

Womack, M., Ziurys, L. M., & Wyckoff, S. 1992, ApJ, 387, 417

Zhou, S. 1992, ApJ, 394, 204

This preprint was prepared with the AAS IATEX macros v5.2.

Table 1. Summary of Single-Dish Telescope Observations

Emission	Rest Frequency (MHz)	Telescope	Receiver	$\theta_{\mathrm{HPBW}}^{\mathrm{a}}$ (arcsec)	$\eta_{ m mb}^{ m \ b}$	$\frac{\Delta v_{\rm res}^{\rm c}}{(\text{km s}^{-1})}$	$\sigma_{\mathrm{T_A^*}}^{\mathrm{d}}$ (mK)	Map ^e Type	Area ^f (arcmin)
NII (1.1)	23694.495	NRO	H22	78	0.82	0.477	46	M/N	E O V E O
NH_3 (1,1)								,	5.9×5.9
NH_3 (2,2)	23722.633	NRO	H22	78	0.82	0.476	56	M/N	5.9×5.9
$NH_3 (3,3)$	23870.130	NRO	H22	78	0.82	0.473	58	M/N	5.9×5.9
$NH_3 (4,4)$	24139.417	NRO	H22	78	0.82	0.469	62	M/N	5.9×5.9
$CC^{34}S 4_3 - 3_2$	44497.559	NRO	S40	40	0.76	0.253	25	D	
$CCS \ 4_3 - 3_2$	45379.033	NRO	S40	40	0.76	0.245	50	M/F	5.3×5.3
$HC^{18}O^{+}$ (1–0)	85162.157	NRO	S80	18.7	0.50	0.130	26	D	
$C_3H_2 \ 2_{12} - 1_{01}$	85338.906	NRO	S100	18.7	0.50	0.130	30	D	
$\mathrm{H}^{13}\mathrm{CO}^{+}\ (1-0)$	86754.330	NRO	S80/S100	18.5	0.50	0.128	37	C/F	3.7×2.4
	86754.330	NRO	BEARS	20.3	0.49	0.108	48	M/F	8.6×8.6
SiO (1–0) $v = 0$	86846.998	NRO	S80	18.5	0.50	0.128	42	M/F	3.7×2.4
	86846.998	NRO	BEARS	20.5	0.49	0.108	185	M/F	8.6×8.6
$N_2H^+(1-0)$	93173.900	NRO	S80/S100	17.2	0.51	0.119	31	M/F	2.0×2.0
$^{12}CO(1-0)$	115271.204	NRO	S100	14.8	0.49	0.0976	94	C/F	2.8×1.8
	115271.204	NRO	BEARS	16.5	0.51	0.0983	139	M/F	7.1×7.1
$^{12}CO(3-2)$	345795.989	CSO		22.0	0.75	0.416	290	M/F	3.7×3.0
$350\mu\mathrm{m}$ continuum	850000	CSO	SHARCII	8.9×8.0					4.0×3.8

^aHalf-power beam width for a circular Gaussian beam

^fSize of the region for the "mapping" observations, and the major and minor axis lengths for "cross scan" ones.

Table 2. Summary of Interferometric Observations

		Center	Synthesized Beam		B 1 1111	Velocity	Image Sensitivity (mJy beam ⁻¹)	
Array	Emission	Frequency (MHz)	i v maj mm		Bandwidth (MHz)	Resolution (km s^{-1})		
VLA	continuum	8435	3.29×2.93	29.7	172 ^a		0.038	
OVRO	continuum	89964	$5.38{ imes}4.80$	41.3	$4096^{\rm b}$		0.15	
	N_2H^+ (1–0)	93173.78	4.91×4.36	-62.4	7.75	0.402	17.6^{c}	
	$\mathrm{H}^{13}\mathrm{CO}^{+}\ (1-0)$	86754.33	$6.31{ imes}4.84$	-24.7	1.938	0.108	33.0^{c}	

^aConcatenated the two polarization data.

^bMain beam efficiency

^cEffective velocity resolution

^dTypical RMS noise level of the spectrum. For detection observations, an RMS noise level of the spectrum is given. For mapping observations, a mean RMS noise level for all the spectra is given.

eObserving modes for the molecular line emission; D denotes "detection" observations toward the center position of R.A.(J2000)= $20^h51^m29.5^s$, Decl.(J2000)= $60^d18'38.0''$, M/F and M/N denote, respectively, "mapping" observations with full-beam and Nyquist sampled grid spacings centered on the above position, and C/F denotes "cross scan" observations with a full-beam spacing along the NE–SW and NW–SE directions centered on the position.

 $^{^{\}rm b}{\rm Concatenated}$ the lower and upper sideband data.

^cPer velocity channel.

Table 3. Summary of the Combined Data from the OVRO MM-Array and the NRO 45 M $\,$ Telescope $^{\rm a}$

Line	Spatial Free $45 \mathrm{m}$ (k λ)	equency Range OVRO (kλ)	Field of View (arcsec)	$\frac{\text{Synthesized}}{\theta_{\text{maj}} \times \theta_{\text{min}}}$ (arcsec)	Beam P.A. (deg)	Velocity Resolution (km s ⁻¹)
$N_2H^+(1-0)$	0.0–5.29	3.30–71.8	69.7	4.49×3.86	-70.7 -27.2	0.402
$H^{13}CO^+(1-0)$	0.0–4.48	3.07–58.0	75.0	6.73×5.14		0.108

^aFor details, see Appendix A

Table 4. Results of Continuum Emission Flux Measurements

λ (μm)	Instruments	struments $\begin{array}{c} { m Size} \\ \hline l_{ m maj} imes l_{ m min} & { m P.A.} \\ ({ m arcsec} imes { m arcsec}) & ({ m deg}) \end{array}$		Peak Intensity (mJy beam ⁻¹)	Total Flux Density (mJy)
35540 3330 350	VLA-D OVRO CSO-SHARCII		 129±17 140±13	< 0.055 1.16 ± 0.17 300 ± 30	0.75±0.07 1830±330

Table 5. Results from the 45 m Telescope Spectral Line Observations: Dense Gas Tracers

Core Center ^a			Inside the Half-Maximum Contour ^b			
Line	$T_{\rm mb}{}^{\rm c}$ (K)	$\Delta v_{\rm int}^{\rm d}$ (km s ⁻¹)	$ au^{ m e}$	$\langle \Delta v_{\rm int} \rangle^{\rm d}$ (km s ⁻¹)	$\langle au angle^{ m e}$	$\langle T_{\rm ex} \rangle$ (K)
N ₂ H ⁺ (1–0)	1.96±0.05	0.35±0.01	3.4±0.08	0.32±0.09	2.7+0.4	9.5±1.9
$H^{13}CO^{+}$ (1–0)	0.88 ± 0.09	0.60 ± 0.03	≤ 0.1	0.52 ± 0.09 0.60 ± 0.17	2.7±0.4	9.5±1.9
$C_3H_2 \ 2_{12} - 1_{01}$ $CCS \ 4_3 - 3_2$	1.12 ± 0.06 0.74 ± 0.07	0.59 ± 0.1 0.41 ± 0.04	$0.34 \\ 0.94$	0.41±0.19		
NH ₃ (1,1)	1.20 ± 0.06	$0.61 {\pm} 0.10$	$1.6 {\pm} 0.1$	$0.62 {\pm} 0.17$	$0.45{\pm}0.18$	≤ 9.7

 $^{^{\}mathrm{a}}$ Single pointing toward the 3 mm continuum source. See the spectra in Figure 2, and beam sizes in Table 1.

^bFor N_2H^+ and NH_3 lines which allow to derive optical depth (τ) and excitation temperature ($T_{\rm ex}$) through hyperfine structure (HFS) analysis, we present mean and standard deviation for the spectra existing inside the half-maximum, i.e., 50% level contour of total integrated intensity map (Figure 4).

 $^{\rm c}$ Peak main-beam brightness temperature. For N₂H⁺ and NH₃ lines, those for the brightest HF components are given.

^dIn calculating intrinsic velocity width ($\Delta v_{\rm int}$), we employed HFS analysis for the N₂H⁺ and NH₃ lines, spectral moment analysis for the H¹³CO⁺ and C₃H₂ lines, and single Gaussian fitting for the CCS line (§4.5.2). For the C₃H₂ and CCS lines, we corrected for line broadening due to the optical depth (Phillips et al. 1969).

 $^{\rm e} \rm Optical~depth.$ We present τ of the brightest hyperfine transition $F_1,F=2,3-1,2$ for N_2H^+ (1–0) (§4.1.1) and $F,F_1=\frac{5}{2},2-\frac{5}{2},2$ for NH $_3$ (1,1) (§4.1.5).

Table 6. Column Densities of N₂H⁺, H¹³CO⁺, C₃H₂, CCS, and NH₃ Molecules^a

	Combined		Nobeyama	45 m Telescope	
Line	Inside $350 \mu\text{m}$ 3σ Contour ^b		Full Extent of		
	3σ Contour	r < 10''	r < 20''	r < 40''	the Core ^d
	(cm^{-2})	(cm^{-2})	(cm^{-2})	(cm^{-2})	(cm^{-2})
N_2H^+	(5.2±2.5)E+13	(5.6±0.2)E+13	(4.4±0.3)E+13	(3.5±0.2)E+13	(3.9±1.0)E+13
$\mathrm{H}^{13}\mathrm{CO}^{+}$	$(4.7\pm0.8)E+11$	$(6.1\pm0.3)E+11$			$(4.3\pm0.2)E+11$
C_3H_2		$(2.4\pm0.3)E+13$			
CCS			$(1.5\pm0.2)E+13$		$(1.5\pm0.3)E+13$
NH_3	• • •			$(8.2 \pm 0.2)E + 14$	$(7.7\pm2.8)E+14$

^aCalculated with the assumption of $T_{\rm ex} = 9.5$ K (§4.1.1)

^cToward the 3 mm continuum source measured with the beam size in Table 1. e.g., $\theta_{\text{HPBW}} = 20''$ beam for the region of $r \leq 10''$. Regarding the N₂H⁺ column densities for the regions of $r \leq 20''$ and 40", we calculate column densities using these spectra smoothed with $\theta_{\text{HPBW}} = 40''$ and 80" beams, respectively (§4.1.1).

 $^{\rm d}$ Measured over the full extent of the core with beam sizes of 20" for N₂H⁺, H¹³CO⁺, and C₃H₂, 40" for CCS, and 80" for NH₃. Here the full extent of the core is defined by a region enclosed by the 50% level contour of each total intensity map.

Table 7. Fractional Abundances of Dense Gas Tracer Molecules

Molecule	$X_{\mathrm{m}}{}^{\mathrm{a}}$	Beam Size (arcsec)	Comments
$^{ m N_2H^+}_{ m H^{13}CO^+}$	(9.5 ± 5.0) E -10 (8.5 ± 4.7) E -12	9×8 9×8	Used $\langle N(\mathrm{H}_2) \rangle^{\mathrm{b}}$ in §3.1.2 Used $\langle N(\mathrm{H}_2) \rangle^{\mathrm{b}}$ in §3.1.2
C_3H_2	$(2\pm1)\text{E}10$	20	$X(N_2H^+)_{8''} \times \frac{N[C_2H_2]}{N[N_2H^+]} (20'')^c$
CCS	(5 ± 3) E -10	40	$X(N_2H^+)_{8''} \times \frac{N[CCS]}{N[N_2H^+]} (40'')^c$
NH_3	$(2\pm1)\text{E8}$	80	$X(N_2H^+)_{8''} \times \frac{N[N_1H_3]}{N[N_2H^+]} (80'')^c$

^aFractional abundance of the molecule.

 $^{^{\}rm b}$ Column densities measured inside an area enclosed by the 3σ level contour of the $350\,\mu{\rm m}$ continuum emission. For this purpose, we made the N₂H⁺ and H¹³CO⁺ maps by giving the SHARC II beam size as a synthesized beam size.

 $[^]b$ We adopted mean H_2 column density, $\langle N(H_2) \rangle$, from cases I and II in §3.1.2 and considered the range of H_2 column densities into the errors in X_m .

 $^{^{\}rm c}$ Assumed that N₂H⁺ does not have radial abundance variation. Column column density ratios are calculated from Table 6. The notation of $X(N_2H^+)_{8}''$ indicates N₂H⁺ abundance measured with the SHARC II beam.

Table 8. LTE and Virial Masses of GF 9-2 Core

	42 16 h		D ($M_{ m vir}{}^{ m d}$		
Line	${\cal A}^{ m a}$ $({ m pc}^2)$	$M_{ m LTE}^{ m b}$ (M_{\odot})	$R_{ m eff}^{ m c}$ (pc)	Case I ^e (M_{\odot})	Case II ^e (M_{\odot})	
N ₂ H ⁺ (1–0)	2.632E-3	1.2 ± 0.7	0.0289	0.39 ± 0.3	0.10 ± 0.08	
$H^{13}CO^{+}$ (1–0)	3.963E-3	1.3 ± 0.3	0.0354	2.9 ± 1.7	$0.12 {\pm} 0.07$	
$CCS \ 4_3 - 3_2$	5.897E-3	$3.1 {\pm} 1.9$	0.0432	$1.7 {\pm} 1.4$	$0.078 {\pm} 0.06$	
$NH_3 (1,1)$	5.544E-3	$4.5 {\pm} 2.4$	0.0419	2.3 ± 1.6	$0.25{\pm}0.15$	

 $^{^{\}mathrm{a}}$ Area enclosed by the 50% level contour of each total integrated intensity map (Figure 4).

dErrors in virial mass are calculated from $(\delta M_{\rm vir})^2 = \left(\frac{\partial M_{\rm vir}}{\partial \langle \Delta v_{\rm int} \rangle}\right)^2 (\delta \langle \Delta v_{\rm int} \rangle)^2 + \left(\frac{\partial M_{\rm vir}}{\partial R_{\rm eff}}\right)^2 (\delta R_{\rm eff})^2$ where $\delta R_{\rm eff}$ and $\delta \langle \Delta v_{\rm int} \rangle$ are those in $R_{\rm eff}$ and $\langle \Delta v_{\rm int} \rangle$, respectively. The intrinsic velocity width $(\Delta v_{\rm int})$ and its error are taken from those for the entire core in Table 5.

^eCases I and II are, respectively, when $\langle \Delta v_{\rm int} \rangle^2 = \langle \Delta v_{\rm thm} \rangle^2 + \langle \Delta v_{\rm turb} \rangle^2$ and $\langle \Delta v_{\rm int} \rangle^2 = \langle \Delta v_{\rm thm} \rangle^2$. Here $\langle \Delta v_{\rm int} \rangle$, $\langle \Delta v_{\rm thm} \rangle$, and $\langle \Delta v_{\rm turb} \rangle$ are means of intrinsic, thermal, and turbulent velocity widths, respectively (see §5.2.1).

^bErrors in LTE-mass include those in the column density, area size, and the abundance.

^cEffective radius defined by $R_{\rm eff} = \sqrt{\mathcal{A}/\pi}$.

Fig. 1.— Overlay of the 3 mm continuum emission map observed with the OVRO mmarray (grey scale plus contours) on the 350 μ m map with the CSO SHARC II camera (thick contours). The contours start from the 3σ levels with a 3σ interval where $\sigma=0.15$ and 29.7 mJy beam⁻¹ for the 3 mm and $350 \,\mu$ m images, respectively. The dashed contours show the -3σ level for the 3 mm image. The $350 \,\mu$ m image does not have negative contours below the -2.2σ level. The ellipses at the bottom corners indicate the beam sizes.

Fig. 2.— Spectra of the molecular line emission shown in the main-beam brightness temperature $(T_{\rm mb})$ scale toward the 3 mm source. The vertical dashed line indicates the systemic velocity $(V_{\rm sys})$ of -2.5 km s⁻¹ (§3.2.1). The horizontal blue and red bars under the ¹²CO lines indicate the LSR-velocity ranges for the integrated intensity maps shown in Figure 8, and the green bars under the N₂H⁺ and H¹³CO⁺ lines are for the maps shown in Figure 6. The N₂H⁺ emission seen in $4.5 \lesssim V_{\rm LSR}/{\rm km~s^{-1}} \lesssim 7.2$ is the main hyperfine components (see Figure 3).

Fig. 3.— N_2H^+ (1–0) spectrum (black histogram) taken with the 45 m telescope toward the 3 mm source. The green histogram represents the best-fit spectrum from the HF analysis (§4.1.1). We assume that the LSR velocity of the isolated $F_1,F=0,1-1,2$ transition ($\nu_{\rm rest}=93176.310~{\rm MHz}$) is equal to the $V_{\rm sys}$ of $-2.5~{\rm km~s^{-1}}$. The lengths of vertical lines above the spectrum indicate the expected relative intensities at $\tau\simeq0$, plotted at the rest frequencies (Cazolli et al. 1985). The horizontal bars below the spectrum show the velocity ranges integrated to obtain maps in Figure 4c and those in the first row of Figure 6.

Fig. 4.— Total integrated intensity maps of the (a) $\mathrm{H}^{13}\mathrm{CO}^{+}$ (1–0), (b) $\mathrm{CCS}\ 4_3-3_2$, (c) $\mathrm{N}_2\mathrm{H}^+$ (1–0), and (d) NH_3 (1,1) lines observed with the 45 m telescope. The velocity ranges for the integrations are between $V_{\mathrm{LSR}} = -2.95$ and -2.1 km s⁻¹ for $\mathrm{H}^{13}\mathrm{CO}^{+}$, and -3.0 and -2.1 km s⁻¹ for CCS . For the $\mathrm{N}_2\mathrm{H}^+$ and NH_3 emission, all the hyperfine emission are integrated over the velocity ranges shown by the horizontal bars in Figures 3 and 10, respectively. Contour intervals are 3σ , starting from the 3σ levels. The 1σ noise levels are 33.4, 42.5, 27.0, and 24.8 mK·km s⁻¹ for the $\mathrm{H}^{13}\mathrm{CO}^+$, CCS , $\mathrm{N}_2\mathrm{H}^+$, and NH_3 maps, respectively. The central star marks the position of the 3 mm source. The hatched circles at the bottom-left corner of each panel show beam size (see Table 1), and the small dots represent the observed grid points.

Fig. 5.— Velocity channel maps of the N_2H^+ (1–0) $F_1,F=0,1-1,2$ and $H^{13}CO^+$ (1–0) emission taken with the 45 m telescope (see Table 1); each panel has a size of $225''\times225''$. The central LSR-velocity for each channel is shown at the upper right corner. Contour intervals are 2σ , starting from the 3σ levels of the images where 1σ noise level is 78 mK in T_{mb} for the N_2H^+ and 96 mK for $H^{13}CO^+$. The star in each panel is the same as in Figure 4. The systemic velocity is $V_{LSR} = -2.5 \text{ km s}^{-1}$.

Fig. 6.— Comparison of the total integrated intensity maps of all the seven hyperfine (HF) emission of N_2H^+ (1–0) (first row), N_2H^+ (1–0) $F_1,F=0,1-1,2$ (second row) emission, and $H^{13}CO^+$ (1–0) (third row) line taken with the Nobeyama 45 m telescope (first column), the OVRO mm-array (second column), and made from the combined 45 m plus OVRO visibilities (third column). The central star and the ellipse at the bottom left corner in each panel are the same as in Figure 4. The large circles in the second and third columns indicate the field of view. The N₂H⁺ total emission maps are integrated over the 3 velocity ranges shown by the horizontal bars in Figure 3, and those for N_2H^+ F_1 , F=0,1-1,2 and $H^{13}CO^+$ maps by the green ones in Figure 2. The contour intervals are the same as in Figure 1. The 1σ rms noise levels are 38.5 mK in $T_{\rm mb}$ for the 45 m N_2H^+ total emission map, 42.5 mK for the 45 m N_2H^+ $F_1,F = 0,1-1,2$ map, 33.5 mK for the 45 m $H^{13}CO^+$ map, 17.4 mJy beam⁻¹ for the OVRO N₂H⁺ total emission image, 22.4 mJy beam⁻¹ for the OVRO $N_2H^+ F_1, F = 0,1-1,2 \text{ image, } 17.2 \text{ mJy beam}^{-1} \text{ for the OVRO } H^{13}CO^+ \text{ image, } 62.4 \text{ mJy beam}^{-1}$ for the combined N₂H⁺ total emission image, 95.5 mJy beam⁻¹ for the combined N₂H⁺ F₁,F = 0,1-1,2 image, and 35.3 mJy beam⁻¹ for the combined H¹³CO⁺ image. The noise levels for the combined data correspond to 170 mK in $T_{\rm sb}$ for the ${\rm H}^{13}{\rm CO}^{+}$, 510 mK for the ${\rm N}_{2}{\rm H}^{+}$ total, and 780 mK for the N_2H^+ $F_1,F=0,1-1,2$ emission maps.

Fig. 7.— Velocity channel maps of the combined OVRO plus 45 m telescope images of the N_2H^+ (1–0) $F_1,F=0,1-1,2$ and $H^{13}CO^+$ (1–0) lines (see Table 3). Contour intervals are the same as in Figure 1, and the RMS noise levels are 32.1 and 52.1 mJy beam⁻¹ for the N_2H^+ and $H^{13}CO^+$ lines, respectively. The size for each channel map is 76″.8×76″.8. The systemic velocity is $V_{LSR} = -2.5$ km s⁻¹.

Fig. 8.— Maps of the blue- (left panels) and redshifted (right panels) 12 CO (1–0) (upper panels) and (3–2) (lower panels) emission. The (1–0) emission is integrated over the velocity ranges of $-4.2 \le V_{\rm LSR}/{\rm km~s^{-1}} \le -3.4$ for the blue and $-1.8 \le V_{\rm LSR}/{\rm km~s^{-1}} \le -1.0$ for the red. The (3–2) emission is integrated in the ranges of $-5.8 \le V_{\rm LSR}/{\rm km~s^{-1}} \le -3.8$ for the blue and $-1.4 \le V_{\rm LSR}/{\rm km~s^{-1}} \le +0.6$ for the red. These velocity ranges are shown in Figure 2. Contours with color scale are drawn by the 10% step up to the 90% level of the peak value. The lowest contour for the (1–0) maps is the 10% level, corresponding to the 21 σ and 8.4 σ levels for the blue and red, respectively. In the (3–2) maps, the lowest contour is the 50% level, corresponding to the 9.0 σ and 8.8 σ levels for the blue and red, respectively. The white dashed contours shown in all the panels indicate the 5 σ level contour of the H¹³CO⁺ total intensity map (Figure 4a), and the inner ones in (c) and (d) indicate the 50% (corresponding to 16.4 σ) level contour. The central circles with a radius of 40" in (a) and (b) show the error circle of the H₂O maser position (Furuya et al. 2003). The central yellow star indicates the position of the 3 mm source. The other symbols are the same as in Figure 4.

Fig. 9.— Column density maps of the N_2H^+ line obtained from (a) the 45 m telescope data and (b) the combined OVRO plus 45 m data (§4.1) in color scale. The color scale bars are the same for both the 45 m and combined data. The black contours in (a) and white ones in (b) indicate the total integrated intensity maps of the N_2H^+ emission (Figure 4c) and the 350 μ m continuum emission (Figure 1), respectively. The white circle in (a) and black one in (b) indicate the OVRO filed of view.

Fig. 10.— NH₃ (1,1) and (2,2) spectra observed with the 45 m telescope toward the 3 mm continuum emission. In the lower panel, the green histogram represents the best-fit NH₃ (1,1) spectrum from the HFS analysis (§4.1.5). It is assumed that the (1,1) and (2,2) spectra have their brightest HF components at $V_{\rm LSR} = -2.5~{\rm km~s^{-1}}$. The vertical lines above the spectra indicate the expected relative intensities at $\tau \simeq 0$ and LSR-velocities of the HF components. The horizontal bars below the (1,1) spectrum show the velocity ranges to obtain the total intensity map shown in Figure 4d.

Fig. 11.— Radial column density profiles of the N₂H⁺ in GF 9-2 core obtained from the Nobeyama 45 m telescope (blue) and the combined OVRO plus 45 m data (black) (see text). The upper horizontal axis shows the linear scale. The right hand vertical axis represents H₂ column density converted with X(N₂H⁺) = 9.5E–10 (Table 7). The solid curves indicate the best-fit power-law profiles (§4.4): $N_{\rm N_2H^+}(r) = (7.3 \pm 1.1) \times 10^{14} (r/1".0)^{-(1.0\pm0.1)}$ cm⁻² for $r \le 50"$ for the combined and $(8.5 \pm 2.5) \times 10^{14} (r/1".0)^{-(1.1\pm0.2)}$ cm⁻² for $r \le 80"$ for the 45 m data. The broken curves indicate the beam patterns: 17".2 in HPBW for the 45 m telescope, and 4".1 for the combined data. The vertical dotted lines at r = 29".9 (corresponding to 0.029 pc) indicates the $R_{\rm eff}$ for the N₂H⁺ core (Table 8).

Fig. 12.— Position-Velocity (PV) diagrams of the N_2H^+ (1–0) $F_1,F=0,1-1,2$ (upper panels) and $H^{13}CO^+$ (1–0) (lower panels) emission for GF 9-2 core made from the 45 m telescope (green contour) and the combined data (greyscale with black contour). The left and right panels, respectively, show the diagrams along the major (P.A.= 45°) and minor (P.A.= 135°) axes, passing through the continuum source. The right hand vertical axis in each panel shows distance from the 3 mm source in pc. The contour intervals are the same as in Figure 4. The intensity is presented in $T_{\rm mb}$ scale for the 45 m and in S_{ν} for the combined data. See the caption of Figure 6 for the RMS noise levels. The vertical and horizontal dotted lines indicate $V_{\rm sys} = -2.5~{\rm km~s^{-1}}$ and the position of the 3 mm source, respectively. The horizontal dashed lines in (c) and (d) running at $\pm 37''.5$ indicate the field of view of the combined data. The horizontal and vertical bars labeled with $V_{\rm res}$ and $\theta_{\rm beam}$ indicate the velocity resolution and beam size, respectively.

Fig. 13.— Intrinsic velocity width $(\Delta v_{\rm int})$ maps (color scale) of (a) N₂H⁺ (1–0) F₁,F=0,1–1,2 and (b) H¹³CO⁺ (1–0) emission for the 45 m telescope data (§4.5.2). The presented $\Delta v_{\rm int}$ ranges are $0.28 \leq \Delta v_{\rm int}/{\rm km~s^{-1}} \leq 0.61$ for the N₂H⁺ and $0.44 \leq \Delta v_{\rm int}/{\rm km~s^{-1}} \leq 0.63$ for the H¹³CO⁺. Contours in (a) and (b) indicate the N₂H⁺ and H¹³CO⁺ total integrated intensity maps shown in Figure 6. The thick white contour in each panel indicates the 50% level contour of the total maps. The star and hatched ellipse are the same as in Figure 4.

Fig. 14.— Plot of normalized CO outflow momentum flux $(F_{\rm CO} \cdot c/L_{\rm bol})$ vs. bolometric temperature $(T_{\rm bol})$ for nearby $(d < 350~{\rm pc})$ low-mass YSOs less luminous than $50L_{\odot}$ (§5.1), including S106 FIR $(L_{\rm bol} \lesssim 1080L_{\odot}; {\rm Richer~et~al.}~1993; {\rm Furuya~et~al.}~2000)$. The filled-and open circles represent the presence and the absence of ${\rm H_2O}$ masers in the period of the Nobeyama survey (Furuya et al. 2001; 2003), respectively. The locus of GF 9-2 $(L_{\rm bol} \simeq 0.3~L_{\odot})$ is indicated by large filled circle. The upper limit in $F_{\rm CO} \cdot c/L_{\rm bol}$ for S106 FIR is recalculated from Furuya et al. (2000) with the 3σ upper limit and the outflow velocity of 50 km s⁻¹. The $T_{\rm bol}$ is taken from Chen et al. (1995) and AWB00, and $F_{\rm CO} \cdot c/L_{\rm bol}$ is calculated from Table 4 in Furuya et al. (2003). The $T_{\rm bol}$ ranges for the class 0, I, and II sources (Chen et al. 1995) are shown by the bottom bars.

Fig. 15.— Map of the intrinsic velocity width of the $H^{13}CO^{+}$ (1–0) emission (greyscale and contour), obtained from the combined data. Contour intervals are the 10% step of the difference between the maximum (0.71 km s⁻¹) and minimum (0.36 km s⁻¹) velocity widths. The thick white and black contours show the 18 σ level of the total integrated intensity map of the combined N_2H^+ data (Figure 6) and the 3 σ level of the 3 mm continuum emission (Figure 1), respectively. The green contours show the highest 3 level contours (18, 21 and 24σ levels) of the total integrated intensity map of the combined $H^{13}CO^{+}$ data (Figure 6). The ellipses are the same as in Figure 4.

Fig. 16.— Upper and lower panels: plots of flux density in Jy vs. projected baseline length in $k\lambda$ for the N₂H⁺ (1–0) line data with the 45 m telescope (filled circles) and the OVRO mm-array (open triangles). The data are from $V_{\rm LSR} = -2.6$ km s⁻¹ channel of the strongest hyperfine component of 1₂₃ – 0₁₂ transition. The lower panel is a magnified plot of the upper one. The visibilities in the plots are resampled with 0.2 and 0.4 $k\lambda$ bins for the 45 m and OVRO data, respectively.

Fig. 17.— Beam patterns (upper panels) and "dirty maps" (lower panels) of the combined N_2H^+ (1–0) data for the robustness powers of +1,0,-1, and -2. The data are from the -2.6 km s⁻¹ channel map of the strongest hyperfine component of $1_{23}-0_{12}$ transition. Contour intervals for the beams are 10% of the peak values, starting from the $\pm 10\%$ levels. Dashed contours are complementary negative contours. Contours in the dirty maps have 3σ steps, starting from the 3σ levels; the 1σ noise levels are 127.5, 82.4, 28.5, and 24.7 mJy beam⁻¹ for the robustness powers of +1, 0, -1, and -2, respectively. The synthesized beam sizes of $\theta_{\rm maj} \times \theta_{\rm min}$ are $10''.33 \times 9''.18, 5''.81 \times 5''.09, 4''.16 \times 3''.57$, and $3''.27 \times 2''.66$ for the robustness powers of +1, 0, -1, and -2, respectively. The central stars in the lower panels represent the position of the 3 mm source.

This figure "f1.jpg" is available in "jpg" format from:

This figure "f2.jpg" is available in "jpg" format from:

This figure "f3.jpg" is available in "jpg" format from:

This figure "f4.jpg" is available in "jpg" format from:

This figure "f5a.jpg" is available in "jpg" format from:

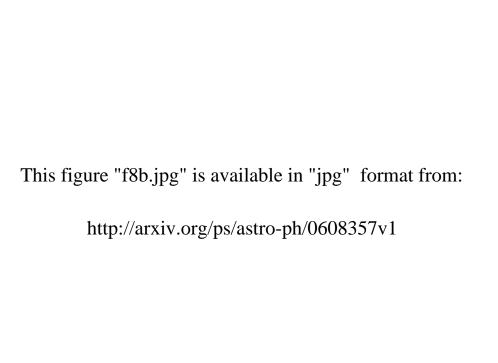
This figure "f5b.jpg" is available in "jpg" format from:

This figure "f6.jpg" is available in "jpg" format from:

This figure "f7a.jpg" is available in "jpg" format from:

This figure "f7b.jpg" is available in "jpg" format from:





This figure "f8c.jpg" is available in "jpg" format from:

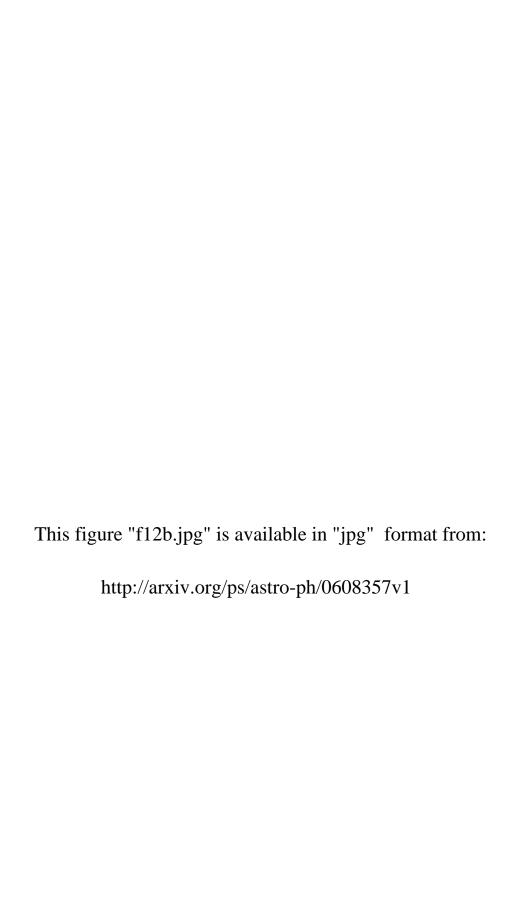
This figure "f8d.jpg" is available in "jpg" format from:

This figure "f9.jpg" is available in "jpg" format from:

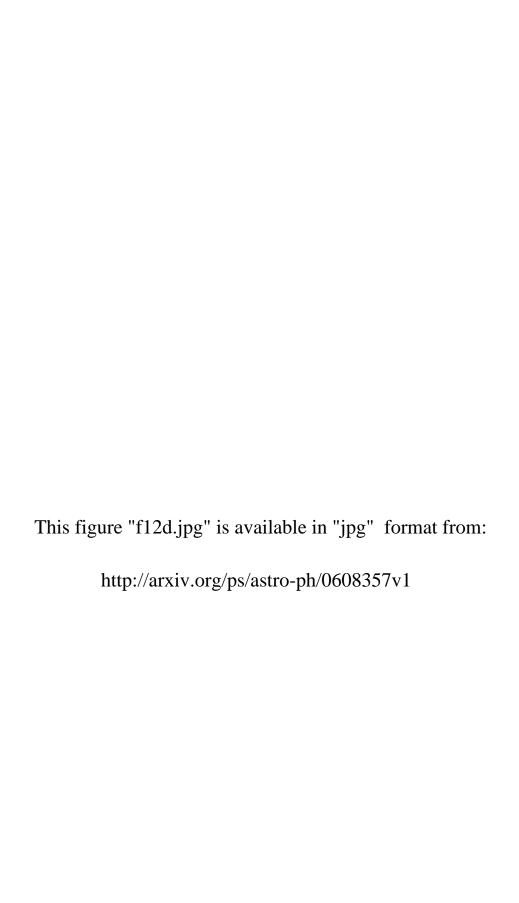
This figure "f10.jpg" is available in "jpg" format from:

This figure "f11.jpg" is available in "jpg" format from:

This figure "f12a.jpg" is available in "jpg" format from: http://arxiv.org/ps/astro-ph/0608357v1



This figure "f12c.jpg" is available in "jpg" format from:



This figure "f13.jpg" is available in "jpg" format from:

This figure "f14.jpg" is available in "jpg" format from:

This figure "f15.jpg" is available in "jpg" format from:

This figure "f16.jpg" is available in "jpg" format from:

This figure "f17.jpg" is available in "jpg" format from: